

**Timing and genesis of Cu–(Au) mineralization in the Khetri Copper Belt,  
northwestern India: constraints from in situ U–Pb ages and Sm–Nd isotopes of  
monazite-(Ce).**

Xiao-Chun Li<sup>a</sup>, Mei-Fu Zhou<sup>a</sup>, A.E. Williams-Jones<sup>b</sup>, Yue-Heng Yang<sup>c</sup>, Jian-Feng  
Gao<sup>d</sup>

*a, Department of Earth Sciences, The University of Hong Kong, Hong Kong SAR,  
China*

*b, Department of Earth and Planetary Sciences, McGill University, Montreal, Canada*

*c, State Key Laboratory of Lithospheric Evolution, Institute of Geology and  
Geophysics, Chinese Academy of Sciences, Beijing, China*

*d, State Key Laboratory of Ore Deposit Geochemistry, Institute of Geochemistry, Chinese  
Academy of Sciences, Guiyang 550002, China*

31

32 **Abstract** The Khetri Copper Belt (KCB) in northwestern India contains a number of  
33 economically important IOCG-like Cu-(Au) deposits hosted in Proterozoic  
34 meta-sedimentary rocks. They comprise massive, vein-type and disseminated  
35 replacement ores with monazite-(Ce) locally present. In this study, *in-situ* U-Pb ages  
36 and Sm-Nd isotopic compositions of monazite-(Ce) were obtained, in order to  
37 constrain the timing of mineralization, and to trace the sources of the ore metals.

38 Monazite-(Ce) crystals were identified in two representative deposits in the KCB,  
39 Madhan-Kudhan and Kolihan. In the Madhan-Kudhan deposit, monazite-(Ce) crystals  
40 from both ores and ore-hosting rocks are intimately intergrown or texturally  
41 associated with hydrothermal minerals (e.g., pyrrhotite, chalcopyrite and biotite), and  
42 are interpreted to have a hydrothermal origin. The hydrothermal monazite-(Ce)  
43 crystals have U-Pb ages of  $833 \pm 5$  to  $837 \pm 6$  Ma, which represent the timing of the  
44 mineralization in the Madhan-Kudhan deposit. Two types of monazite-(Ce) crystals  
45 were observed in the sample of the Kolihan deposit. Type 1 monazite-(Ce) crystals  
46 occur in close spatial association with sulfide minerals, indicating a hydrothermal  
47 origin. Uranium-lead dating of these monazite-(Ce) crystals yielded an age of  $840 \pm 6$   
48 Ma, which is indistinguishable from the U-Pb ages of hydrothermal monazite-(Ce)  
49 from the Madhan-Kudhan deposit. Type 2 monazite-(Ce) crystals are enclosed by  
50 sulfide minerals, and commonly show concentric zonation with respect to ThO<sub>2</sub> (0.45  
51 to 13.59 wt.%). They yielded a weighted average  $^{207}\text{Pb}/^{206}\text{Pb}$  age of  $1362 \pm 29$  Ma and  
52 an upper concordia intercept age of  $1357 \pm 30$  Ma, which may record a pre-ore  
53 metamorphic event in the KCB. Hydrothermal monazite-(Ce) crystals have  
54  $\varepsilon_{\text{Nd}}(t=835\text{Ma})$  values ranging from -4.3 to -16.8, indicating the incorporation in the  
55 ore-forming systems of a range of upper crustal materials with different isotopic  
56 signatures.

57 The mineralization ages of the Cu-(Au) deposits in the KCB fall within the  
58 overall age-ranges of the regional post-collisional igneous activity (~800 to ~880 Ma)  
59 and Ca-Na metasomatism (~830 to ~850 Ma). Combining this temporal association  
60 with related geochemical and isotopic data, we propose that the Neoproterozoic

post-collisional magmatism induced large scale circulation of non-magmatic hydrothermal fluids in the upper crust, which produced widespread Ca-Na metasomatism and led to the mobilization and concentration of certain ore-metals (e.g., REE, and partial Cu).

**Key words:** Monazite-(Ce), U-Pb dating, Sm-Nd isotopes, Neoproterozoic, Khetri Copper Belt

## 1. Introduction

Several Cu ± Au ± Fe ± REE ± U deposits are hosted in late Paleoproterozoic meta-sedimentary rocks of Aravalli-Delhi Fold Belt, northwestern India, which is also referred as the Khetri Copper Belt (KCB). These deposits host ~140 Mt ore @ 1.1 to 1.7 wt.% Cu and 0.5 g/t Au, making the KCB one of the largest Cu metallogenic provinces in India (Knight, 2002). An early model proposed a syngenetic origin for the deposits, in which the ores were formed during sedimentation or diagenesis and were subsequently metamorphosed (Sarkar and Dasgupta, 1980). Another early model, which still has adherents, proposed that the mineralization formed epigenetically, and was possibly associated genetically with regional magmatism (e.g., Das Gupta, 1974; Kaur et al., 2014). Recent studies, however, have emphasized the Iron Oxide Copper Gold (IOCG)-like affinity of the deposits (Knight 2002; Baidya et al., 2017).

Establishing the timing of mineralization in the KCB is key to understanding the ore genesis. A mean fission track age of  $897 \pm 125$  Ma was reported for garnet from a representative deposit in the KCB (Knight 2002 and reference therein), and has been proposed to represent the timing of Cu mineralization. However, garnet is a metamorphic mineral rather than an ore-related hydrothermal mineral in the deposit, and thus its fission track age could not represent the age of ore formation. Moreover, the large uncertainty in the age determination makes it of questionable use even in constraining the age of the metamorphism. In order to properly constrain the ore-forming age, it is necessary to select ore-related minerals and to use robust

isotopic methods that will yield age determinations with relatively small uncertainty. It is well established that monazite can form during hydrothermal ore-forming processes (e.g., VMS-type deposits, [Davis et al., 1994](#); Sn-porphyry deposits, [Kempe et al., 2008](#); orogenic gold deposits, [Rasmussen et al., 2006](#), [Vielreicher et al., 2015](#); magmatic-hydrothermal REE deposits, [Pandur et al., 2016](#)). Hydrothermal monazite commonly contains high U and/or Th concentrations, but negligible common Pb, and its U-Th-Pb systems have closure temperatures greater than 700 °C ([Williams et al., 2007](#); [Chiaradia et al., 2013](#)). Thus, it is an ideal phase for determining the mineralization age of hydrothermal deposits.

Monazite is excellent not only for U-Th-Pb dating but also for Sm-Nd isotopic analysis due to its high concentrations of Sm and Nd. Advances in microanalysis now permit submineral-scale determination of Sm-Nd isotopic compositions (e.g., [Fisher et al., 2011](#); [Liu et al., 2012](#); [Goudie et al., 2014](#)). Importantly, the micro-analysis of Sm-Nd isotopes may reveal isotopic heterogeneities within and between single grains (e.g., [Gregory et al., 2009a](#); [Fisher et al., 2017](#)), which were obscured by conventional whole-rock isotopic analysis.

In this study, we report textural features and compositions of monazite-(Ce) from two representative deposits in the KCB, and demonstrate that monazite-(Ce) is an ore-related hydrothermal mineral. *In-situ* U-Pb and Sm-Nd isotopic analyses were conducted on the hydrothermal monazite-(Ce). The new dataset provides direct constraints on the timing of the Cu mineralization and the sources of REE in the ores, and hence a better understanding of the origin of the Cu mineralization in the KCB.

## 2. Regional Geology

The Aravalli-Delhi Fold Belt represents a major NE-SW tectonic lineament in the northwestern part of the Indian subcontinent ([Fig. 1a](#)). The oldest rock unit of this belt is the Banded Gneissic Complex (BGC), which has been divided into two disconnected terranes, namely the BGC-I in the southern Aravalli mountains and BGC-II in the central Aravalli mountains ([Fig. 1b](#); [Heron, 1953](#)). The BGC-I unit is

dominated by a tonalite-trondhjemite-granodiorite suite of Archean age (3.30 to 2.50 Ga; Wiedenbeck and Goswami, 1994; Roy and Kröner, 1996; Wiedenbeck et al., 1996), whereas the BGC-II unit mainly comprises Archean to Paleoproterozoic (2.75 to 1.72 Ga) granitoids and Paleoproterozoic supra-crustal rocks (Buick et al., 2006; Dharma Rao et al., 2011).

The BGC is in tectonic contact with, or unconformably overlain by two Proterozoic supracrustal sequences, namely the Aravalli and Delhi Supergroups. Both supracrustal sequences were deposited during episodes of continental rifting (e.g., Singh, 1988; Bhattacharya and Bull, 2010). The Aravalli Supergroup is widely distributed in the eastern and southeastern segments of the Aravalli-Delhi Fold Belt along a NE-SW trending basin (Fig. 1b). This supergroup consists mainly of greenschist- to amphibolites-facies siliciclastic rocks and carbonates, with mafic volcanic rocks, phosphorite and VMS-type Pb-Zn deposits distributed locally (Sinha-Roy et al., 1998). Previous geochronological studies indicate that the Aravalli sedimentation spanned the time interval from ~2.3 to ~1.6 Ga (Ahmad et al., 2008; McKenzie et al., 2013).

The Delhi Supergroup forms the dominant lithostratigraphic unit of the Aravalli mountains. This supergroup has been divided into two sub-belts, namely the North Delhi Fold Belt, and the South Delhi Fold Belt (Fig. 1b). The North Delhi Fold Belt hosts a succession of amphibolite-facies meta-sediments, comprising the quartzite-dominated Alwar Group and the schist-dominated Ajabgarh Group. These sedimentary rocks were deposited at < 1.71 Ga (Deb and Sarkar, 1990; Kaur et al., 2011a, 2013). The South Delhi Fold Belt consists of quartzite, schist, meta-conglomerate, carbonates and minor meta-volcanic rocks, which have been tightly folded into a regional synclinorium and metamorphosed up to amphibolite facies (Heron, 1953; Gupta 1998). The depositional age of these rocks is estimated at 1.2 to 1.0 Ga (Deb et al., 2001; McKenzie et al., 2013).

Closure of the Delhi basin is marked by the ~1.0 to ~0.9 Ga collision between the Marwar Craton in the west and the Bundelkhand Craton in the east (Vijaya Rao et al., 2000; Bhowmik et al., 2010; Fig. 1a). This event is recorded by evidence of

151 metamorphism in the central and northern domains of the Aravalli-Delhi Fold Belt  
152 (e.g., [Pant et al., 2008](#); [Bhowmik et al., 2010](#); [Hazarika et al., 2013](#); [Ozha, 2016](#)), and  
153 localized magmatism in the southern domain of this Fold Belt (e.g., [Deb et al., 2001](#);  
154 [Pandit et al., 2003, 2011](#)). Post-collisional intrusions, termed “Erinpura Granites”,  
155 occur widely in the southern segment of the Aravalli-Delhi Fold Belt ([Fig. 1b](#); [Heron,](#)  
156 [1953](#)). The Erinpura Granites include variably deformed felsic intrusions composed of  
157 granite, tonalite, diorite and granitic gneisses.

158 To the northwest of the Erinpura Granites lies the ~770 to ~750 Ma Malani  
159 Igneous Suite, which consists dominantly of unmetamorphosed rhyolitic and  
160 rhyodacitic volcanic rocks, with minor basalts and granitic intrusions ([Torsvik et al.,](#)  
161 [2001](#); [Gregory et al., 2009b](#); [Fig. 1b](#)). The Malani Igneous Suite has been interpreted  
162 as having formed in an Andean-type arc setting (e.g., [Ashwal et al., 2002](#); [Meert et al.,](#)  
163 [2013](#)), or an extensional setting (e.g., active rifting or mantle plume; [Eby and Kochhar,](#)  
164 [1990](#); [Li et al., 1999](#); [Sharma, 2004](#)).

165

### 166 **3. The Khetri Copper Belt**

167

168 The NE-SW oriented KCB is located in the northernmost part of the  
169 Aravalli-Delhi Fold Belt ([Fig. 1b](#)). Large Cu-(Au) deposits occur near the Towns of  
170 Khetri and Gothra, including from northeast to southwest the Banwas,  
171 Madhan-Kudhan, Kolihan, Chandmari Intervening Block and Chandmari deposits  
172 ([Fig. 2a](#)). It is estimated that the Banwas deposit contains 30 Mt ore @ 1.7 Cu and 0.3  
173 to 3 g/t Au, the Madan-Kudan deposit contains 66 Mt ore @ 1.12 to 1.71 wt.% Cu and  
174 0.2 to 2 g/t Au, the Kolihan-Chandmari deposit contains 40 Mt ore @ 1.14 to 1.62 wt.%  
175 Cu and 0.2 g/t Au, and the Chandmari Intervening Block contains 12.10 Mt ore @  
176 1.03 wt.% Cu ([Knight et al. 2002](#); [Bhardwaj et al., 2014](#)). The Madan-Kudan and  
177 Kolihan deposits are currently being mined.

178 The KCB mineral deposits are hosted in meta-sedimentary rocks of the Alwar  
179 and Ajabgarh Groups. They occur over a >10 km curvilinear NE-strike length, which  
180 is generally parallel to a boundary marking the transition from the meta-sedimentary

rocks (dominantly amphibole-bearing quartzite and feldspathic quartzite; Figs. 3a and b) of the Alwar Group to the east, to rocks (dominantly garnet-chlorite schist, andalusite-/biotite-schist, phyllite and garnet-bearing quartzite; Fig. 3c) of the Ajabgarh Group to the west. Sedimentary structures in the Alwar and Ajabgarh Groups have been interpreted to reflect shelf/shallow marine to fluvial environments (Singh, 1988; Deb and Sarkar, 1990). A regionally-continuous, stratigraphically-conformable breccia horizon occurs at the contact between the Alwar and Ajabgarh Groups (Fig. 3d). The breccias are interpreted to have formed by evaporate dissolution (Knight et al., 2002 and references therein). The meta-sedimentary rocks of the Alwar and Ajabgarh Groups have experienced at least two phases of regional metamorphism; the peak metamorphic conditions were 500 to 600 °C and < 5.5 kb (Sarkar and Dasgupta, 1980; Kaur et al., 2016). The last metamorphic event has been interpreted to have taken place at 975 to 945 Ma using chemical dating of monazite (Pant et al., 2008; Kaur et al., 2016). A number of granitic intrusions are present in the KCB, including the ~1.82 Ga subduction-related granites and 1.72 to 1.70 Ga rift-related A-type granites (Kaur et al., 2007, 2009b, 2011b; Fig. 2a).

Sedimentary rocks of the KCB have experienced widespread calc-silicate alteration and/or albite-hematite alteration (Knight et al., 2002; Kaur et al., 2016). The calc-silicate alteration comprises assemblages of amphibole, clinopyroxene, scapolite, albite and calcite, with variable epidote, apatite, titanite and iron oxides. Albite-hematite alteration was characterized by the formation of mainly albite, amphibole, magnetite and hematite, and is responsible for the red color of the altered rocks. In addition to the meta-sedimentary rocks, the 1.72 to 1.70 Ga A-type granites also experienced variable degrees of albite alteration, during which hydrothermal fluids converted plagioclase and K-feldspar into nearly pure albite (Kaur et al., 2012; 2014).

Two main phases of deformation have been identified in the KCB, namely earlier ductile deformation and later brittle or brittle-ductile deformation (Knight et al., 2002). Rocks in this belt commonly display a sub-vertical, NE-striking foliation, defined by

211 peak metamorphic minerals, and steeply plunging mineral lineations. The foliation is  
212 axial-planar to NE-trending on a regional-scale. Doubly-plunging folds are observed.  
213 These early structures were cross-cut by NE- and NW-striking brittle faults or shear  
214 zones. The Cu-(Au) ores occur mainly along the NE-striking, west-dipping fault  
215 zones or shear zones, forming a series of discontinuous, sub-parallel lenses (Figs. 2b  
216 and c). In places, orebodies also occur at the intersections of NE- and NW-striking  
217 faults, forming subvertical cylindrically-shaped bodies, or in the hinges of small-scale  
218 fault-related folds (Roy Chowdhury and Das Gupta, 1965).

219 Sulfide mineralization occurs in the form of massive bodies (Figs. 3e and f),  
220 veins (Fig. 3g), and disseminations (Fig. 3h). Sulfide-rich masses are preferentially  
221 developed in the main orebodies, whereas sulfide-bearing veins and sulfide  
222 disseminations are more abundant in the hanging wall and footwall alteration zones.  
223 Chalcopyrite and pyrrhotite are the dominant sulfide minerals within the main  
224 orebodies, and are accompanied by subordinate pyrite (Figs. 4a and b). Magnetite is  
225 the dominant iron oxide phase (Figs. 4a). Minor proportions of uraninite, huttonite  
226 and REE-rich phases (e.g., allanite-(Ce), monazite-(Ce) and xenotime-(Y)) are also  
227 present (Fig. 4c). The ore-related gangue minerals are amphibole, marialitic scapolite,  
228 biotite, chlorite and quartz (Figs. 4d to e), with subordinate albite, tourmaline, apatite  
229 and carbonate minerals. Both ore and gangue minerals show little evidence of  
230 deformation (Figs. 4a to e). Sulfide-bearing veins generally cross-cut the peak  
231 metamorphic fabric or foliation of the ore-hosting rocks (Fig. 3g). Thus, the  
232 mineralization is interpreted to have postdated the main phases of regional  
233 metamorphism and deformation, consistent with the conclusions of previous studies  
234 (Knight et al., 2002).

235 Wallrock alteration is well developed on the orebody-scale, with amphibole,  
236 biotite, chlorite, quartz and carbonate minerals as the most common alteration phases.  
237 The amphibole alteration typically extends for hundreds of meters away from the  
238 orebodies. Amphibole in the alteration zone has variable major element compositions,  
239 and mainly includes cummingtonite, hastingsite, sadanagaite, and tschermakite. For  
240 simplicity, the latter three are referred to as Ca-group amphibole. Cummingtonite



commonly occurs as randomly oriented crystals cross-cutting the peak metamorphic fabric (Fig. 4f). The Ca-group amphibole is paragenetically later than the cummingtonite, and occurs as randomly oriented crystals, patches or layers in the ore-hosting rocks (Fig. 4g). Biotite and chlorite alteration is developed adjacent to the main orebodies (usually tens of meters away). These minerals occur generally along fractures or grain boundaries, and may define the schistosity of the ore-hosting rocks (Figs. 4h and i). Quartz occurs either as patches overprinting the meta-sedimentary rocks, or as veins cutting through or paralleling the metamorphic fabric. The silicification may extend for hundreds of meters away from the main ore bodies. Carbonate minerals commonly occur as veins cutting through the metamorphic fabric. Although the above-mentioned alteration may have resulted from the hydrothermal fluids responsible for mineralization, it is not invariably accompanied by sulfide minerals.

254

#### 255 **4. Sample description**

256

257 In this study, monazite-(Ce) from four samples was investigated in detail. Three  
258 samples (In-123, In-125 and In-103) were collected from the Madhan-Kudhan deposit,  
259 and one (In-192) was from the Kolihan deposit.

260

##### 261 **4.1 Sample In-123**

262

263 Sample In-123 is a massive ore that was collected from the 0 meter level of the  
264 Madhan-Kudhan mine (Fig. 5). This sample mainly contains cummingtonite (10  
265 vol.%), magnetite (30 vol.%), sulfide minerals (chalcopyrite and pyrrhotite; 30 vol.%)  
266 and biotite (25 vol.%), with minor relict quartzite masses. Cummingtonite was the  
267 earliest mineral to crystallize, and commonly forms aggregates unevenly distributed  
268 through the sample (Fig. 6a). The later magnetite occurs either as irregularly shaped  
269 crystals overprinting cummingtonite, or as large independent crystals/aggregates up to  
270 5 mm in length (Figs. 6a to c). Sulfide minerals are closely associated with biotite.

271 The sulfide-biotite assemblage commonly forms the matrix to the large magnetite  
272 crystals/aggregates (Figs. 6b and c).

273 Monazite-(Ce) mostly occurs in clusters with more than 10 grains (Fig. 6d).  
274 Locally, it is isolated. In both cases, monazite-(Ce) shows a close spatial association  
275 with sulfide minerals and biotite. Dark pleochroic halos were observed at the contacts  
276 between monazite-(Ce) and biotite. Individual monazite-(Ce) crystals are euhedral to  
277 subhedral in shape, and relatively uniform in size (100 to 200  $\mu\text{m}$  in length) (Figs. 6e  
278 and f). Sulfide minerals may occur as inclusions in some monazite-(Ce) crystals (Figs.  
279 6e and f).

280

#### 281 4.2 Sample In-125

282

283 Sample In-125 is a massive ore that was collected from the -60 meter level of the  
284 Madhan-Kudhan mine. It consists mainly of cummingtonite (15 vol.%), magnetite (20  
285 vol.%), tourmaline (10 vol.%), sulfide minerals (chalcopyrite and pyrrhotite; 30 vol.%)  
286 and biotite (20 vol.%), with minor relict quartz. The earliest cummingtonite  
287 commonly occurs as randomly oriented tabular crystals. Magnetite is present as  
288 irregularly-shaped crystals that overprint cummingtonite (Fig. 7a), as euhedral to  
289 subhedral inclusions in tourmaline (Figs. 7b and c), and as independent crystals of  
290 variable size (Fig. 7d). Tourmaline commonly appears as large ( $> 150 \mu\text{m}$  in length),  
291 disseminated crystals that are closely associated with magnetite (Fig. 7b). Sulfide  
292 minerals are intimately intergrown with biotite. They were the latest minerals to form,  
293 and overprint cummingtonite, magnetite and tourmaline (Fig. 7c).

294 Monazite-(Ce) crystals are euhedral to subhedral in shape, and vary widely in  
295 grain size (100  $\mu\text{m}$  to 600  $\mu\text{m}$  in length) (Figs. 7d to f). They are generally  
296 disseminated and occur in close spatial association with sulfide minerals and biotite,  
297 i.e., they are in planar to irregular contact with sulfide minerals and/or biotite, and  
298 may contain inclusions of sulfide mineral and/or biotite (Figs. 7d to f). Where  
299 monazite-(Ce) is in contact with biotite, dark pleochroic halos can be observed around  
300 the monazite-(Ce) crystals. Locally, monazite-(Ce) occurs in contact with magnetite,

301 tourmaline and zircon (Figs. 7d and f).

302

#### 303 4.3 Sample In-103

304

305 Sample In-103 is a sedimentary rock that hosts ore, and was collected at the 0  
306 meter level of the Madhan-Kudhan mine (Fig. 5). This sample has experienced  
307 intensive biotite alteration, during which the primary rock-forming minerals and  
308 textures were almost totally obliterated (Fig. 8). In addition to biotite, this sample also  
309 contains minor tourmaline, apatite and allanite-(Ce), which form relatively large,  
310 disseminated crystals in the biotite matrix (Fig. 8a). Sulfide disseminations and  
311 veinlets are observed locally (Fig. 8a).

312 Monazite-(Ce) commonly occurs in clusters of 5 to 10 crystals within the biotite  
313 matrix; the crystals vary greatly in size ( $< 10\ \mu\text{m}$  to  $> 100\ \mu\text{m}$  in length) even within  
314 the same cluster (Figs. 8b and c). Dark pleochroic halos are developed at the contacts  
315 between monazite-(Ce) and biotite. Some monazite-(Ce) crystals contain inclusions of  
316 xenotime-(Y) or sulfide minerals (Fig. 8d).

317

#### 318 4.4 Sample In-192

319

320 Sample In-192 is a massive ore that was collected from an ore pile at the Kolihan  
321 mine. This sample mainly comprises magnetite (30 vol.%), sulfide minerals  
322 (pyrrhotite and minor chalcopyrite; 40 vol.%) and chlorite (25 vol.%), which are  
323 accompanied by subordinate scapolite, apatite and relict quartz. Magnetite is present  
324 either as single crystals or aggregates, and was overprinted by later-stage sulfide  
325 minerals and chlorite (Fig. 9a). Scapolite and apatite occur as disseminated grains in  
326 association with either early magnetite or late sulfide minerals and chlorite (Fig. 9b).

327 Two types of monazite-(Ce) crystals were observed in this sample. Type 1  
328 monazite-(Ce) crystals have planar to irregular contacts with sulfide minerals and  
329 chlorite, and they usually contain inclusions of sulfide minerals, chlorite and/or tiny  
330 Th-rich phases (Figs. 9c to e). They commonly have irregular shapes, and their grain

sizes is variable (30 to 80  $\mu\text{m}$  in length). In BSE images, they appear homogeneous. Type 2 monazite-(Ce) occurs as inclusions in sulfide minerals (Figs. 9f to h). They are typically rounded to sub-rounded, and relatively uniform in size (40 to 60  $\mu\text{m}$  in length). In contrast to Type 1 crystals, they do not contain sulfide mineral or chlorite inclusions, but may host some quartz inclusions. The above observations suggest that Type 2 crystals pre-dated Type 1 crystals.

## 5. Analytical methods

### 5.1 Electron microprobe analyses

The composition of monazite-(Ce) was analyzed using a JEOL JXA-8100 electron microprobe at The University of Hong Kong. The analyses were performed using a 20 kV accelerating voltage and a 20 nA beam current. The beam spot diameter was set at 1  $\mu\text{m}$ . The analyzing crystals were PET (P, U, Th, Y, Ca and Cl), LIF (La, Ce, Pr, Nd, Sm, Eu, Gd, Tb, Dy, Ho, Er, Tm, Yb and Lu), LDE1 (F), and TAP (Si and Na). The  $K\alpha$  line was chosen for the analyses of P, Si, Ca, Na, F and Cl. The  $L\alpha$  line was chosen for La, Ce and Y, the  $L\beta$  line for Pr, Nd, Sm, Eu, Gd, Tb, Dy, Ho, Er, Tm, Yb and Lu, and the  $M\alpha$  line for Th and U. The counting times of peaks were 8 s for F, Cl and Na, 30 s for P, La, Ce, Pr and Nd, and 60 s for other elements. Background intensities were measured on both sides of the peak for half of the peak counting time. The standards were apatite for P, uraninite for U, huttonite for Th, hornblende for Si and Ca, monazite for La, Ce, Pr, Nd and Sm, synthesized  $\text{EuF}_3$  for Eu, synthesized REE metals for Gd, Tb, Dy, Ho, Er, Tm, Yb and Y, and albite for Na, topaz for F, and tugtupite for Cl. All data were corrected using standard ZAF correction procedures. The EMPA data are summarized in Table 1, and the whole dataset can be found in Supplemental Material.

### 5.2 Monazite-(Ce) U-Pb isotopic determinations

Monazite-(Ce) U-Pb isotopic determinations were made using an Agilent ICP-MS, equipped with a Geolas 193 nm excimer laser ablation system at the Institute of Geology and Geophysics, Chinese Academy of Sciences (IGGCAS). The analytical procedure follows that described by Liu et al. (2012). The monazite-(Ce) grains were analyzed in thin sections. Before analysis, transmitted and reflected photomicrographs, and BSE images were used to check for inclusions, cracks, and zoning. Analyses were performed with a spot size of 32  $\mu\text{m}$  and a repetition rate of 5 Hz. Helium was used as the carrier gas and was mixed with argon prior to entering the ICP torch. Each spot analysis involved approximately 20 s of background data acquisition and 50 s of sample data acquisition. The external standard 44069 ( $^{207}\text{Pb}/^{206}\text{Pb} = 0.05532$ ,  $^{207}\text{Pb}/^{235}\text{U} = 0.5195$  and  $^{206}\text{Pb}/^{238}\text{U} = 0.06811$ ; Aleinikoff et al., 2006) was used to correct for the U/Pb fractionation and the instrumental mass discrimination for monazite-(Ce) in samples In-123 and In-192. In the case of samples In-103 and In-125, the external standard was M4 ( $^{207}\text{Pb}/^{206}\text{Pb} = 0.05794$ ,  $^{207}\text{Pb}/^{235}\text{U} = 0.6671$  and  $^{206}\text{Pb}/^{238}\text{U} = 0.08384$ ; Liu et al., 2012). The raw count of  $^{204}\text{Pb}$  was nearly zero, so common Pb corrections were not made. The data reduction was carried out using the software package ICPMSDataCal (Liu et al., 2008). The Namaqua-1 monazite was used as an external standard to monitor the accuracy of the analytical procedure. Seven spots yielded a weighted mean  $^{206}\text{Pb}/^{238}\text{U}$  age of  $527 \pm 5$  Ma ( $2\sigma$ ), which is consistent, within uncertainty, with the reported value of  $523 \pm 4$  Ma (Liu et al., 2012). The U-Pb age data are listed in Table 2.

382

### 383 5.3 *In-situ* Sm-Nd isotopic analysis

384

Monazite-(Ce) crystals from the Kolihan deposit are commonly small ( $< 50 \mu\text{m}$  in length), so after LA-ICP-MS U-Pb age determination, they were not suitable for Sm-Nd isotopic analyses. Consequently, these analyses were only conducted on monazite-(Ce) from the Madhan-Kudhan deposit. The analyses were performed using a Neptune multi-collector (MC) ICP-MS, equipped with a Geolas 193 nm excimer laser ablation system at IGGCAS. The details of the analytical procedures were

described by Liu et al. (2012) and Yang et al. (2014). The analyses were conducted on thin sections, with a spot size of 20  $\mu\text{m}$  and a repetition rate of 4 Hz. Each spot analysis involved  $\sim 20$  s of background data acquisition and  $\sim 40$  s of data acquisition from the sample. After analyses of eight samples, two Namaqua monazite standards were measured for external calibration, utilizing the reference values:  $^{147}\text{Sm}/^{144}\text{Nd}$ :  $0.0977 \pm 0.0002$ ;  $^{143}\text{Nd}/^{144}\text{Nd}$ :  $0.511896 \pm 0.000032$  (Liu et al., 2012). The isobaric interference of  $^{144}\text{Sm}$  on  $^{144}\text{Nd}$  is significant. In order to correct for this interference, we used the measured  $^{147}\text{Sm}/^{149}\text{Sm}$  ratio to calculate the Sm fractionation factor, and then used the measured  $^{147}\text{Sm}$  intensity and the natural  $^{147}\text{Sm}/^{144}\text{Sm}$  ratio to estimate the Sm interference on mass 144. The interference-corrected  $^{146}\text{Nd}/^{144}\text{Nd}$  ratio was then used to calculate the Nd fractionation factor. Finally, the  $^{143}\text{Nd}/^{144}\text{Nd}$  and  $^{145}\text{Nd}/^{144}\text{Nd}$  ratios were normalized using the exponential law. The  $^{147}\text{Sm}/^{144}\text{Nd}$  ratio was calculated after correcting for the isobaric interference of  $^{144}\text{Sm}$  on  $^{144}\text{Nd}$  as described above, and then was externally calibrated against the  $^{147}\text{Sm}/^{144}\text{Nd}$  ratio of the Namaqua reference monazite. The raw data were exported offline and the whole data-reduction procedure was performed using an in-house Excel VBA (Visual Basic for Applications) macro program. The monazite standard 44069 was measured as an external standard to monitor the accuracy of the analytical procedure, yielding weighted mean  $^{147}\text{Sm}/^{144}\text{Nd}$  and  $^{143}\text{Nd}/^{144}\text{Nd}$  ratios of  $0.1168 \pm 0.0022$  and  $0.51217 \pm 0.00001$ , respectively. These values are consistent, within uncertainty, with the reported values of  $0.1159 \pm 0.0064$  and  $0.512175 \pm 0.000040$ , respectively (Liu et al., 2012). The *in-situ* Sm-Nd isotopic data are listed in Table 3.

413

## 414 6. Analytical results

415

### 416 6.1 Composition of monazite-(Ce)

417

Monazite-(Ce) from sample In-103, In-125 and Type 1 monazite-(Ce) crystals from sample In-192 are generally homogeneous in composition. They are rich in LREE, with Ce predominant, and are predictably depleted in HREE. They have a

ThO<sub>2</sub> content ranging from 0.16 to 3.42 wt.%, but mostly lower than 2 wt. %, and contain minor proportions of CaO (< 0.74 wt.%) and SiO<sub>2</sub> (0.09 to 0.63 wt.%). Thus, there are minor huttonite (ThSiO<sub>4</sub>) and brabantite (CaTh(PO<sub>4</sub>)<sub>2</sub>) components in these crystals.

Monazite-(Ce) crystals from sample In-123 are compositionally heterogeneous, especially with respect to La<sub>2</sub>O<sub>3</sub> (11.27 to 19.46 wt.%), Nd<sub>2</sub>O<sub>3</sub> (10.42 to 17.77 wt.%) and Sm<sub>2</sub>O<sub>3</sub> (1.19 to 5.43 wt.%). In addition to the LREE<sub>2</sub>O<sub>3</sub>, they also contain minor proportions of ThO<sub>2</sub> (0.06 to 2.72 wt.%), CaO (0.11 to 0.63 wt.%), and SiO<sub>2</sub> (< 0.15 wt.%).

Type 2 monazite-(Ce) crystals from sample In-192 show large ranges in P<sub>2</sub>O<sub>5</sub> (26.01 to 30.71 wt.%), La<sub>2</sub>O<sub>3</sub> (12.08 to 18.10 wt.%), Ce<sub>2</sub>O<sub>3</sub> (22.33 to 28.74 wt.%), ThO<sub>2</sub> (0.45 to 13.59 wt.%) and SiO<sub>2</sub> (0.04 to 2.55 wt.%). It is notable that there is a positive correlation between (Th + U + Si) (a.p.f.u.) and (REE + Y + P) (a.p.f.u.) (Fig. 10a), indicating that Th<sup>4+</sup> is charge-balanced through the coupled substitutions of Th<sup>4+</sup> + Ca<sup>2+</sup> = 2(REE+Y)<sup>3+</sup> and Th<sup>4+</sup> + Si<sup>4+</sup> = P<sup>5+</sup> + (REE+Y)<sup>3+</sup>.

## 6.2 Monazite-(Ce) U-Pb ages

Twenty-two analyses were conducted on sixteen monazite-(Ce) crystals from sample In-123. All the measured ratios plot on or near concordia, and yielded a weighted average <sup>206</sup>Pb/<sup>238</sup>U age of 833 ± 5 Ma (MSWD = 3.2) (Fig. 11a).

A similar number of analyses (twenty-four on fifteen monazite-(Ce) crystals) were carried out for sample In-125. All the analyses yielded concordant/sub-concordant ages, which form a coherent cluster on concordia (with a weighted average <sup>206</sup>Pb/<sup>238</sup>U age of 836 ± 7 Ma; MSWD = 3.9) (Fig. 11b).

Twenty analyses were conducted on seventeen monazite-(Ce) crystals from sample In-103. Nineteen of the analyses yielded concordant/sub-concordant results with a coherent cluster on concordia, corresponding to a weighted average <sup>206</sup>Pb/<sup>238</sup>U age of 837 ± 6 Ma (MSWD = 2.6) (Fig. 11c). One analysis (In-103-20) yielded an obviously discordant age, and was not considered in the age calculation (Fig. 11c).

For sample In-192, nine spots were analyzed on nine Type 1 monazite-(Ce) crystals. Eight concordant analyses clustered tightly on concordia, and yielded a weighted average  $^{206}\text{Pb}/^{238}\text{U}$  age of  $840 \pm 6$  Ma (MSWD = 0.85) (Fig. 11d). One analysis was obviously discordant, and yielded an older  $^{207}\text{Pb}/^{206}\text{Pb}$  age (Fig. 11d). This analysis was probably conducted on an older monazite-(Ce) crystal that had experienced Pb-loss. We also conducted ten analyses on ten Type 2 monazite-(Ce) crystals. These analyses yielded a wide range of apparent Pb/U ages, with  $^{207}\text{Pb}/^{235}\text{U}$  ages varying from 1304 to 1441 Ma, and  $^{206}\text{Pb}/^{238}\text{U}$  ages from 1288 to 1496 Ma. However, the  $^{207}\text{Pb}/^{206}\text{Pb}$  ages form a tight cluster, yielding a weighted average value of  $1362 \pm 29$  Ma (MSWD = 0.21). These analyses define a regression line with an upper concordia intercept at  $1357 \pm 30$  Ma (MSWD = 0.21) (Fig. 11e). This age distribution suggests that the different Type 2 monazite-(Ce) crystals may have formed at approximately the same time ( $\sim 1360$  Ma), but experienced variable degrees of post-crystallization Pb-loss and/or U-loss (Williams, 1998).

### 6.3 *In-situ* Sm-Nd isotopic composition

Monazite-(Ce) crystals from sample In-123 have large ranges in  $^{147}\text{Sm}/^{144}\text{Nd}$  (0.1343 to 0.1946) and  $^{143}\text{Nd}/^{144}\text{Nd}$  (0.51173 to 0.51239) ratios. In comparison, the crystals from sample In-125 have smaller ranges in  $^{147}\text{Sm}/^{144}\text{Nd}$  (0.1337 to 0.1561) and  $^{143}\text{Nd}/^{144}\text{Nd}$  (0.51182 to 0.51200); the corresponding ratios for In-103 are relatively uniform (0.1117 to 0.1185 and 0.51132 to 0.51136, respectively). Overall,  $^{147}\text{Sm}/^{144}\text{Nd}$  correlates positively with  $^{143}\text{Nd}/^{144}\text{Nd}$  (Fig. 12a).

## 7. Discussion

### 7.1 The hydrothermal origin of monazite-(Ce) and timing of Cu-(Au) mineralization

The U-Pb isotopic age determinations reported above indicate that, except for one sample, all the monazite-(Ce) crystals analyzed formed between  $833 \pm 5$  Ma and



840  $\pm$  6 Ma. The exception is sample In-192 from the Kolihan deposit, which, in addition to monazite-(Ce) crystals in this age range, contains a second, texturally earlier, population (Type 2) that yielded a weighted average  $^{207}\text{Pb}/^{206}\text{Pb}$  age of  $1362 \pm 29$  Ma and an upper concordia intercept age of  $1357 \pm 30$  Ma. These ages are within the age range (1.37 to 1.33 Ga) recently reported for a metamorphic event in the central part of the Aravalli-Delhi Fold Belt (Hazarika et al., 2013; Ozha et al., 2016). We therefore propose that the Type 2 monazite-(Ce) crystals in sample In-192 may be of metamorphic origin, and record a pre-mineralization metamorphic event in the northern part of this belt.

In contrast to Type 2 monazite-(Ce) crystals, Type 1 monazite-(Ce) crystals in sample In-192 and monazite-(Ce) in the other samples occur in contact with, and/or contain inclusions of sulfide minerals, biotite and/or chlorite, indicating that monazite-(Ce) grew synchronously with and/or slightly post-dated these minerals (there is no evidence that they grew along healed fractures). As sulfides, biotite and chlorite are major constituents of the ores, it therefore follows that the monazite-(Ce) crystals formed hydrothermally and the corresponding U-Pb ages record the timing of Cu-(Au) mineralization.

Our U-Pb data show that hydrothermal monazite-(Ce) crystals from the Madhan-Kudhan and Kolihan deposits have indistinguishable U-Pb ages ( $833 \pm 5$  to  $837 \pm 7$  Ma; and  $840 \text{ Ma} \pm 6 \text{ Ma}$ , respectively), indicating that Cu-(Au) mineralization in the two deposits was coeval. Considering that the other deposits in the KCB have very similar structural, alteration and mineralization styles to the Madhan-Kudhan and Kolihan deposits, we propose that all the deposits in the belt have the same age, i.e., they formed at  $\sim 835$  Ma.

505

## 7.2 Sources of REE

507

At the time of mineralization, the  $\epsilon_{\text{Nd}}(t)$  values of hydrothermal monazite-(Ce) varied from -4.3 to -16.8, with an average value of -9.6 (Fig. 12b). These values indicate that the REE in the ores were predominantly of crustal origin. Possible crustal

sources for the REE include syn-ore crustally-derived magmas, meta-sedimentary rocks of the Alwar and Ajabgarh Groups and Paleoproterozoic felsic intrusions. No syn-ore crustally-derived intrusions were found in the mining areas, but sparse granitic intrusions that are broadly coeval with the Cu-(Au) mineralization have been reported from northern domain of the Aravalli-Delhi Fold Belt, including the 820 Ma Jhunjhunu intrusion and the 818 to 817 Ma Tosham intrusions (Kaur et al., 2013 and references therein). Thus, it is possible that there are some hidden syn-ore intrusions beneath the deposits. Unfortunately, there are no Sm-Nd isotopic data available for the intrusions broadly coeval with the mineralization, so it is uncertain if REE, or some of them, were derived from syn-ore magmas. It should be noted that the time-evolved  $\epsilon_{\text{Nd}}$  array of the Paleoproterozoic intrusions in the region generally overlaps with the  $\epsilon_{\text{Nd}}$  range of the monazite-(Ce) at the time of mineralization (Fig. 12b). This overlap is consistent with an input of REE from certain altered Paleoproterozoic intrusions. There are no Sm-Nd isotopic data available for the meta-sedimentary rocks in the region, but the meta-sedimentary rocks predictably maintain evolved Nd isotopic compositions. As such, it is possible that the metasedimentary rocks were also important sources of the REE. It is also necessary to note that the Nd isotopic compositions of hydrothermal monazite-(Ce) are highly heterogeneous between or within single samples. Such heterogeneity may reflect involvement and mixing of a range of crustal materials with different isotopic signatures.

531

### 7.3 A possible genetic linkage between Cu-(Au) mineralization and regional magmatism and metasomatism

534

As mentioned above, some granitic intrusions that are broadly coeval with the Cu-(Au) mineralization occur in the northern domain of the Aravalli-Delhi Fold Belt. This Neoproterozoic magmatic event is more firmly established in the southern domain of the Aravalli-Delhi Fold Belt, represented by the post-collisional Erinpura Granites (Fig. 1). Rubidium-strontium isochrones initially established the age of the Erinpura Granites as being in the range of 830 to 820 Ma (Choudhary et al., 1984).

541 More precise zircon and monazite U-Pb ages, however, have extended the age range  
 542 from 873 to 800 Ma (Fig. 13). Significantly, the KCB was subjected to regional  
 543 Ca-Na metasomatism within this time interval, as evidenced by a titanite U-Pb age of  
 544  $847 \pm 8$  Ma for a metasomatic rock containing an assemblage of  
 545 albite-hematite-amphibole-calcite-titanite, and a whole-rock-mineral Sm-Nd isochron  
 546 age of  $831 \pm 15$  Ma for an altered mafic rock (Fig. 13). It had been assumed that there  
 547 was a broad synchronicity between regional metasomatism and Cu-(Au)  
 548 mineralization in the KCB (Knight et al., 2002; Kaur et al., 2014), but there has been  
 549 no convincing evidence to support it. The geochronological data presented in this  
 550 study demonstrate that the Cu-(Au) mineralization was indeed temporally associated  
 551 with regional Ca-Na metasomatism, as well as the post-collisional magmatism.

552 The temporal association between Cu-(Au) mineralization and regional  
 553 magmatism and metasomatism may imply a genetic linkage between them.  
 554 Magmatism usually plays an important role in the formation of iron oxide-bearing  
 555 Cu-Au deposits. It may provide ore-forming fluids and ore metals for the  
 556 mineralization directly (e.g., Sillitoe, 2003; Baker et al., 2008; Rieger et al., 2010),  
 557 and/or act as heat engines to drive non-magmatic fluids (e.g., basinal brines, seawater  
 558 and meteoric water) involved in the ore-forming process (Barton and Johnson, 1996;  
 559 Xavier et al., 2008; Williams et al., 2010). Baidya et al. (2017) reported that the  
 560 ore-related amphibole from the Kolihan deposit has high content of Cl (2.4 to 6.2  
 561 wt.%). Although the content of Cl in amphibole is controlled by many factors, such  
 562 high Cl-contents can only be explained by equilibration of the amphibole with a  
 563 hydrothermal fluid having high Cl activity (Kullerud and Erambert, 1999; Xiao et al.,  
 564 2005; Liu et al. 2009). This is consistent with the common occurrence of marialitic  
 565 scapolite in ores and the presence of high salinity fluid inclusions (~50 wt.% NaCl  
 566 equivalent; Jaireth, 1984) in ore-related quartz. Fluids with high chlorinity may be of  
 567 magmatic origin and/or result from the dissolution of evaporites. Sulfide minerals,  
 568 including pyrrhotite, chalcopyrite and pyrite, from Madhan-Kudhan and Kolihan  
 569 deposits have  $\delta^{34}\text{S}_{\text{VCDT}}$  values ranging from +7.1 to +13.1‰, with an average value of  
 570 +10.4‰ (our unpublished data). The presence of pyrrhotite in the ore indicates that

571 oxygen fugacity was low, and that H<sub>2</sub>S was the dominant dissolved sulfur species. The  
572  $\delta^{34}\text{S}$  values of the bulk fluid were therefore calculated assuming that the sulfur is  
573 present as H<sub>2</sub>S. These values were calculated from the sulfur isotopic compositions of  
574 the ore minerals to be +7.0 to +12.9‰, assuming a temperature of 375 °C (a common  
575 temperature for the deposition of chalcopyrite in magmatic hydrothermal systems;  
576 [Hezarkhani et al., 1999](#); [Landtwing et al., 2005](#)). These values are higher than those of  
577 typical magma-derived sulfur, but are similar to those of sulfur from many  
578 sedimentary rocks ([Ohmoto and Rye, 1979](#); [Seal, 2006](#)). Thus, we speculate that the  
579 ore-forming fluids were, at least in part, derived from the dissolution of evaporite or  
580 represent bittern basinal brines. Similar fluid sources have been proposed by [Baidya](#)  
581 [et al. \(2017\)](#), based on the composition of ore-related amphibole. As Cl is an effective  
582 ligand for the mobilization of metals like Cu, Au (at high temperature) and the REE  
583 ([Williams-Jones and Migdisov, 2014](#) and references therein), circulation of  
584 chloride-rich fluids would have led to extensive leaching of these metals and their  
585 transport into the ore-forming system. Indeed, geochemical analyses have  
586 demonstrated that sodic metasomatism of the 1.72 to 1.70 Ga A-type granites was  
587 accompanied by considerable leaching of Fe, U and REE from the granites due to the  
588 breakdown of the mafic and accessory phases ([Kaur et al., 2014](#)). Our Sm-Nd isotopic  
589 data also imply that the Paleoproterozoic igneous intrusions and/or meta-sedimentary  
590 rocks could have been important contributors of REE to the ores.

591 Based on the above-mentioned lines of evidence, we propose that  
592 Neoproterozoic magmatism induced circulation of non-magmatic Cl-rich fluids in the  
593 upper crust (e.g., evaporate-derived fluids and/or bittern basinal brines). Interaction of  
594 these fluids with meta-igneous and meta-sedimentary rocks would have produced  
595 widespread Ca-Na metasomatism, and at the same time leached considerable amounts  
596 of ore metals from the altered rocks. Some of the Cu and Au may have gone to form  
597 Cu-(Au) ores. It is unclear whether magmatic-hydrothermal fluids were also involved  
598 in the ore-forming process, and, if so, what their roles were in the mineralization.  
599 Further geochemical and isotopic studies are needed to resolve these issues.

600

## 601    **8. Conclusions**

602

603    (1) The Madhan-Kudhan and Kolihan deposits of the KCB contain syn-ore  
604    hydrothermal monazite-(Ce). Hydrothermal monazite-(Ce) from the two deposits  
605    yielded U-Pb ages of  $833 \pm 5$  to  $840 \pm 6$  Ma, interpreted to represent the timing of  
606    Cu-(Au) mineralization in the KCB.

607    (2) The Kolihan deposit also contains a subset of monazite-(Ce) crystals with an age  
608    of  $\sim 1.36$  Ga. They may record a previously unidentified metamorphic event in the  
609    KCB.

610    (3) REE and, by inference, other metals in the ores may have been derived, at least in  
611    part, from a range of upper crustal rock units with different isotopic signatures.

612    (4) The Cu-(Au) mineralization in the KCB was broadly coeval with regional  
613    post-collisional magmatism and Ca-Na metasomatism. The magmatism may have  
614    been an important source of energy for the mineralization. Regional-scale  
615    metasomatism may lead to the mobilization of certain ore metals in the upper crust,  
616    and facilitated the formation of the Cu-(Au) ores.

617

## 618    **Acknowledgements**

619

620        We would like to express our great thanks to Mr. Singh A.K., Mr. Biswaranjan P.,  
621    and Mr. Mishra V.N. of the Khetri Copper Mine for their kind help during the field  
622    work. We are grateful to Dr. Jingyuan Chen from Chang'an University for his help  
623    with data collection. This study was supported by a grant from State Key Laboratory  
624    for Mineral Deposits Research, Nanjing University (21-16-01), and a grant from Key  
625    Laboratory of Mineralogy and Metallogeny, Guangzhou Institute of Geochemistry  
626    (KLMM20150205).

627

## 628    **References**

629

630    Ahmad, T., Dragusanu, C., and Tanaka, T., 2008, Provenance of Proterozoic Basal Aravalli mafic

631 volcanic rocks from Rajasthan, Northwestern India: Nd isotopes evidence for enriched mantle  
632 reservoirs: *Precambrian Research*, v. 162, p. 150-159.

633 Aleinikoff, J.N., Schenck, W.S., Plank, M.O., Srogi, L., Fanning, C.M., Kamo, S.L., and  
634 Bosbyshell, H., 2006, Deciphering igneous and metamorphic events in high-grade rocks of the  
635 Wilmington Complex, Delaware: morphology, cathodoluminescence and backscattered electron  
636 zoning, and SHRIMP U-Pb geochronology of zircon and monazite: *Geological Society of  
637 America Bulletin*, v. 118, p. 39-64.

638 Ashwal, L.D., Demaiffe, D., and Torsvik, T.H., 2002, Petrogenesis of Neoproterozoic granitoids  
639 and related rocks from the Seychelles: the case for an Andean-type arc origin: *Journal of  
640 Petrology*, v. 43, p. 45-83.

641 Baidya, A.S., Paul, J., Pal, D.C., and Upadhyay, D., 2017, Mode of occurrences and geochemistry  
642 of amphibole in the Kolihan-Chandmari copper deposits, Rajasthan, India: insight into the  
643 ore-forming process: *Ore Geology Reviews*, v. 80, p. 1092-1110.

644 Baker, T., Mustard, R., Fu, B., Williams, P.J., Dong, G., Fisher, L., Mark, G., and Ryan, C.G.,  
645 2008, Mixed messages in iron oxide-copper-gold systems of the Cloncurry district, Australia:  
646 Insight from PIXE analyses of halogens and copper in fluid inclusions: *Mineralium Deposita*, v.  
647 43, p. 559-608.

648 Barton, M.D., and Johnson, D.A., 1996, Evaporitic-source model for igneous related Fe  
649 oxide-(REE-Cu-Au-U) mineralization: *Geology*, v. 24, p. 259-262.

650 Bhardwaj, R., Singh, A.K., and Mishra, V.N., 2014, Exploration for copper ore in Chandmari  
651 Intervening Block, Khetri Copper Belt, Rajasthan. 34<sup>th</sup> Annual Day and National Seminar,  
652 conference paper.

653 Bhattacharya, H.N., and Bull, S., 2010, Tectono-sedimentary setting of the Paleoproterozoic  
654 Zawar Pb-Zn deposits, Rajasthan, India: *Precambrian Research*, v. 177, p. 323-338.

655 Bhowmik, S.K., Bernhardt, H.J., and Dasgupta, S., 2010, Grenvillian age high-pressure upper  
656 amphibolite-granulite metamorphism in the Aravalli-Delhi mobile belt, northwestern India: new  
657 evidence from monazite chemical age and its implication: *Precambrian Research*, v. 178, p.  
658 168-184.

659 Buick, I.S., Allen, C., Pandit, M., Rubatto, D., and Hermann, J., 2006, The Proterozoic magmatic

660 and metamorphic history of the Banded Gneiss Complex, central Rajasthan, India: LA-ICP-MS  
661 U–Pb zircon constraints: *Precambrian Research*, v. 151, p. 119-142.

662 Chen, W.T., Zhou, M.F., Li, X., Gao, J.F., and Hou, K., 2015, In-situ LA-ICP-MS trace elemental  
663 analyses of magnetite: Cu-(Au, Fe) deposits in the Khetri copper belt in Rajasthan Province,  
664 NW India: *Ore Geology Reviews*, v. 65, p. 929-939.

665 Chiaradia, M., Schaltegger, U., Spikings, R., Wotzlaw, J.F., and Ovtcharova, M., 2013, How  
666 accurately can we date the duration of magmatic-hydrothermal events in porphyry systems?-An  
667 invited paper: *Economic Geology*, v. 108, p. 565-584.

668 Choudhary, A.K., Gopalan, K., and Anjaneya Sastry, C., 1984, Present status of geochronology of  
669 the Precambrian rocks of Rajasthan: *Tectonophysics*, v. 105, p. 131-140.

670 Das Gupta, S.P., 1974, Geological setting and origin of sulphide deposits in the Khetri copper belt,  
671 Rajasthan: *Bulletin Geological, Mining and Metallurgical Society of India*, v. 47, p. 221-238.

672 Davis, D.W., Schandl, E.S., and Wasteneys, H.A., 1994, U-Pb dating of alteration around massive  
673 sulfide deposits in the Superior province, Canada: *Contributions to Mineralogy and Petrology*, v.  
674 115, p. 427-437.

675 Deb, M., and Sarkar, S.C., 1990, Proterozoic tectonic evolution and metallogenesis in the  
676 Aravalli-Delhi orogenic complex, northwestern India: *Precambrian Research*, v. 46, p. 115-137.

677 Deb, M., Thorpe, R.I., Kristic, D., Corfu, F., and Davis, D.W., 2001, Zircon U-Pb and galena Pb  
678 isotope evidence for an approximate 1.0 Ga terrane constituting the western margin of the  
679 Aravalli-Delhi orogenic belt, northwestern India: *Precambrian Research*, v. 108, p. 195-213.

680 Dharma Rao, C.V., Santosh, M., Purohit, R., Wang, J., Jiang, X., and Kusky, T., 2011, LA-ICP-MS  
681 U-Pb zircon age constraints on the Paleoproterozoic and Neoproterozoic history of the Sandmata  
682 Complex in Rajasthan within the NW Indian Plate: *Journal of Asian Earth Sciences*, v. 42, p.  
683 286-305.

684 Eby, G.N., and Kochhar, N., 1990, Geochemistry and petrogenesis of the Malani igneous suite,  
685 North Peninsular India: *Journal of the Geological Society of India*, v. 36, p. 109-130.

686 Fisher, C.M., McFarlane, C.R.M., Hanchar, J.M., Schmitz, M.D., Sylvester, P.J., Lam, R., and  
687 Longerich, H.P., 2011, Sm-Nd isotope systematics by laser ablation-multicollector-inductively  
688 coupled plasma mass spectrometry: Methods and potential natural and synthetic reference  
689 materials: *Chemical Geology*, v. 284, p. 1-20.

690 Fisher, C.M., Hanchar, J.M., Miller, C.F., Phillips, S., Vervoort, J., and Whitehouse, M.J., 2017,  
 691 Combining Nd isotopes in monazite and Hf isotopes in zircon to understand complex  
 692 open-system processes in granitic magmas: *Geology*, v. 45(4).

693 Goudie, D.J., Fisher, C.M., Hanchar, J.M., Crowley, J.L., and Ayers, J.C., 2014, Simultaneous in  
 694 situ determination of U-Pb and Sm-Nd isotopes in monazite by laser ablation ICP-MS:  
 695 *Geochemistry Geophysics Geosystems*, v. 15, p. 2575-2600.

696 Gregory, C.J., McFarlane, C.R.M., Hermann, J., and Rubatto, D., 2009a, Tracing the evolution of  
 697 calcalkaline magmas: in-situ Sm-Nd isotope studies of accessory minerals in the Bergell  
 698 Igneous Complex, Italy: *Chemical Geology*, v. 260, p. 73-86.

699 Gregory, L.C., Meert, J.G., Bingen, B., Pandit, M.K., and Torsvik, T.H., 2009b, Paleomagnetism  
 700 and geochronology of the Malani Igneous Suite, Northwest India: implications for the  
 701 configuration of Rodinia and the assembly of Gondwana: *Precambrian Research*, v. 170, p.  
 702 13-26.

703 Gupta, P., Guha, D.B., and Chattopadhyay, B., 1998, Basement-cover relationship in the Khetri  
 704 Copper Belt and the emplacement mechanism of the granite massifs, Rajasthan: *Journal of the*  
 705 *Geological Society of India*, v. 52, p. 417-432.

706 Harlov, D.E., Wirth, R., and Hetherington, C.J., 2011, Fluid-mediated partial alteration in  
 707 monazite: the role of coupled dissolution-reprecipitation in element redistribution and mass  
 708 transfer: *Contribution to Mineralogy and Petrology*, v. 162, p. 329-348.

709 Hazarika, P., Upadhyay, D., and Mishra, B., 2013, Contrasting geochronological evolution of the  
 710 Rajpura-Dariba and Rampura-Agucha metamorphosed Zn-Pb deposit, Aravalli-Delhi Belt, India:  
 711 *Journal of Asian Earth Sciences*, v. 73, p. 429-439.

712 Heron, A.M., 1953, *The Geology of Central Rajputana: Memoirs of the Geological Survey of*  
 713 *India* 79, 339pp.

714 Hezarkhani, A., Williams-Jones, A.E., and Gammons, C.H., 1999, Factors controlling copper  
 715 solubility and chalcopyrite deposition in the Sungun porphyry copper deposit, Iran: *Mineralium*  
 716 *Deposita*, v. 34, p. 770-783.

717 Jaireth, S., 1984, Ore paragenesis and fluid inclusion thermometry of copper sulphide ores from  
 718 Madan-Kudan and Kolihan deposits: *Special Publication Geological Survey of India*, v. 12, p.  
 719 551-568.



720 Just, J., Schulz, B., de Wall, H., Jourdan, F., and Pandit, M.K., 2011, Monazite CHIME/EPMA  
 721 dating of Drinpura granitoid deformation: implications for Neoproterozoic tectono-thermal  
 722 evolution of NW India: *Gondwana Research*, v. 19, p. 402-412.

723 Kaur, P., Chaudhri, N., Raczek, I., Kröner, A., and Hofmann, A.W., 2007, *Geochemistry, zircon*  
 724 *ages and whole-rock Nd isotopic systematics for Palaeoproterozoic A-type granitoids in the*  
 725 *northern part of the Delhi belt, Rajasthan, NW India: implications for late Palaeoproterozoic*  
 726 *crustal evolution of the Aravalli craton: Geological Magazine*, v. 144, p. 361-378.

727 Kaur, P., Chaudhri, N., Raczek, I., Kröner, A., and Hofmann, A.W., 2009, Record of 1.82 Ga  
 728 Andean-type continental arc magmatism in NE Rajasthan, India: insights from zircon and  
 729 Sm-Nd ages, combined with Nd-Sr isotope geochemistry: *Gondwana Research*, v. 16, p. 56-71.

730 Kaur, P., Zeh, A., Chaudhri, N., Gerdes, A., and Okrusch, M., 2011a, Archaean to  
 731 Palaeoproterozoic crustal evolution of the Aravalli orogen, NW India, and its hinterland: the  
 732 U-Pb and Hf isotope record of detrital zircon: *Precambrian Research*, v. 187, p. 155-164.

733 Kaur, P., Chaudhri, N., Raczek, I., Kröner, A., Hofmann, A.W., and Okrusch, M., 2011b, Zircon  
 734 ages of late Palaeoproterozoic (ca. 1.72-1.70 Ga) extension-related granitoids in NE Rajasthan,  
 735 India: regional and tectonic significance: *Gondwana Research*, v. 19, p. 1040-1053.

736 Kaur, P., Chaudhri, N., Hofmann, A.W., Raczek, I., Okrusch, M., Skora, S., and Baumgartner, L.P.,  
 737 2012, Two-stage, extreme albitization of A-type granites from Rajasthan, NW India: *Journal of*  
 738 *Petrology*, v. 53, p. 919-948.

739 Kaur, P., Chaudhri, N., Hofmann, A.W., Raczek, I., and Okrusch, M., 2013, *Geochemistry and*  
 740 *Sm-Nd geochronology of the metasomatised mafic rocks in the Khetri complex, Rajasthan, NW*  
 741 *India: evidence of an Early Cryogenian metasomatic event in the northern Aravalli orogen:*  
 742 *Journal of Asian Earth Sciences*, v. 62, p. 401-413.

743 Kaur, P., Chaudhri, N., Hofmann, A.W., Raczek, I., Okrusch, M., Skora, S., and Koepke, J., 2014,  
 744 Metasomatism of ferroan granites in the northern Aravalli orogen, NW India: geochemical and  
 745 isotopic constraints, and its metallogenic significance. *International Journal of Earth Sciences*, v.  
 746 103, p. 1083-1112.

747 Kaur, P., Zeh, A., Okrusch, M., Chaudhri, N., Gerdes, A., and Bratz, H., 2016, Separating regional  
 748 metamorphic and metasomatic assemblages and events in the northern Khetri complex, NW  
 749 India: Evidence from mineralogy, whole-rock geochemistry and U-Pb monazite chronology:

Journal of Asian Earth Sciences, v. 129, p. 117-141.

Kempe, U., Lehmann, B., Wolf, D., Rodionov, N., Bombach, K., Schwengfelder, U., and Dietrich, A., 2008, U-Pb SHRIMP geochronology of Th-poor, hydrothermal monazite: An example from the Llallagua tin-porphyry deposit, Bolivia: *Geochimica et Cosmochimica Acta*, v. 72, p. 4352-4366.

Knight, J., Lowe, J., Joy, S., Cameron, J., Merrillees, J., Nag, S., Shah, N., Dua, G., and Jhala, K., 2002, The Khetri Copper Belt, Rajasthan: iron oxide copper-gold terrane in the Proterozoic of NW India, in Porter, T.M., e.d., *Hydrothermal iron oxide copper-gold & related deposits: a global perspective*, volume 2: Adelaide, PGC Publishing, p. 321-341.

Kullerød, K., and Erambert, M., 1999, Cl-scapolite, Cl-amphibole, and plagioclase equilibria in ductile shear zones at Nusfjord, Lofoten, Norway: implications for fluid compositional evolution during fluid-mineral interaction in the deep crust: *Geochimica et Cosmochimica Acta*, v. 63, p. 3829-3844.

Landtwing, M.R., Pettke, T., Halter, W.E., Heinrich, C.A., Redmond, P.B., Einaudi, M.T., and Kunze, K., 2005, Copper deposition during quartz dissolution by cooling magmatic-hydrothermal fluids: The Bingham porphyry: *Earth and Planetary Science Letters*, v. 235, p. 229-243.

Liu, J., Liu, W., Ye, K., and Mao, Q., 2009, Chlorine-rich amphibole in Yangkou eclogite, Sulu ultrahigh-pressure metamorphic terrane, China: *European Journal of Mineralogy*, v. 21, p. 1265-1285.

Liu, Z.C., Wu, F.Y., Yang, Y.H., Yang, J.H. and Wilde, S.A., 2012, Neodymium isotopic compositions of the standard monazites used in U-Th-Pb geochronology: *Chemical Geology*, v. 334, p. 221-239.

Li, Z.X., Li, X.H., Kinny, P.D., and Wang, J., 1999, The breakup of Rodinia: did it start with a mantle plume beneath South China? *Earth and Planetary Science Letters*, v. 173, p. 171-181.

McKenzie, N.R., Hughes, N.C., Myrow, P.M., Banerjee, D.M., Deb, M., and Planavsky, N.J., 2013, New age constraints for the Proterozoic Aravalli-Delhi successions of India and their implications: *Precambrian Research*, v. 238, p. 120-128.

Meert, J.G., Pandit, M.K., and Kameirov, G.D., 2013, Further geochronological and paleomagnetic constraints on Malani (and pre-Malani) magmatism in NW India: *Tectonophysics*, v. 608, p.

780 1254-1267.

781 Ohmoto, H., and Rye, R.O., 1979, Isotopes of sulfur and carbon, in Barnes, H.L., ed.,  
 782 Geochemistry of hydrothermal ore deposits, 2nd ed.: New York, Wiley-Interscience, p. 509-567.

783 Ozha, M.K., Mishra, B., Hazarika, P., Jeyagopal, A.V., and Yadav, G.S., 2016, EPMA monazite  
 784 geochronology of the basement and supracrustal rocks within PurBanera basin, Rajasthan:  
 785 evidence of Columbia breakup in northwestern India: *Journal of Asian Earth Sciences*, v. 117, p.  
 786 284-303.

787 Pandey, M., Pant, N.C., and Kumar, S., 2013, Criteria to distinguish between regional and contact  
 788 zone monazite-a case study from Proterozoic North Delhi Fold Belt (NDFB), India: *Episodes*, v.  
 789 36, p. 275-289.

790 Pandit, M.K., Carter, L.M., Ashwal, L.D, Tucker, R.D., Torsvik, T.H., Jamtveit, B., and Bhushan,  
 791 S.K., 2003, Age, petrogenesis and significance of 1 Ga granitoids and related rocks from the  
 792 Sendra area, Aravalli Craton, NW India: *Journal of Asian Earth Sciences*, v. 22 p. 363-381.

793 Pandit, M.K., Wall, H., Daxberger, H., Just, J., Bestmann, M., and Sharma, K.K., 2011, Mafic  
 794 rocks from Erinpura gneiss terrane in the Sirohi region: Possible ocean-floor remnants in the  
 795 foreland of the Delhi Fold Belt, NW India: *Journal of Earth System Science*, v. 120, p. 627-641.

796 Pandur, K., Ansdell, K.M., Kontak, D.J., Halpin, K.M., and Creighton, S., 2016, Petrographic and  
 797 mineral chemical characteristics of the Hoidas Lake Deposit, Northern Saskatchewan, Canada:  
 798 constraints on the origin of a distal magmatic-hydrothermal REE system: *Economic Geology*, v.  
 799 111, p. 667-694.

800 Pant, N.C., Kundu, A., and Joshi, S., 2008, Age of metamorphism of Delhi Supergroup rocks –  
 801 electron microprobe ages from Mahendragarh district, Haryana: *Journal of the Geological*  
 802 *Society of India*, v. 72, p. 365-372.

803 Rasmussen, B., Sheppard, S., and Fletcher, I.R., 2006, Testing ore deposit models using in situ  
 804 U-Pb geochronology of hydrothermal monazite: Paleoproterozoic gold mineralization in  
 805 northern Australia: *Geology*, v. 34, p. 77-80.

806 Rieger, A.A., Marschik, R., Díaz, M., Hölzl, S., Chiaradia, M., Akker, B., and Spangenberg, J.E.,  
 807 2010, The hypogene IOCG mineralization in the Mantoverde district, northern Chile: *Economic*  
 808 *Geology*, v. 105, p. 1271-1299.

809 Roy Chowdhury M.K., and Das Gupta S.P., 1965, Ore-localization in the Khetri Copper Belt,

810 Rajasthan, India: *Economic Geology*, v. 60, p. 69-88.

811 Roy, A.B., and Kröner, A., 1996, Single zircon evaporation ages constraining the growth of the

812 Archaean Aravalli craton, northwestern Indian shield: *Geological Magazine*, v. 133, p. 333-342.

813 Sarkar, S.C., and Dasgupta, S., 1980, Geologic Setting, genesis and transformation of the sulfide

814 deposits in the northern part of the Khetri copper belt, Rajasthan, India -an outline: *Mineralium*

815 *Deposita*, v. 15, p. 117-137.

816 Schandl, E.S., and Gorton, M.P., 2004, A textural and geochemical guide to the identification of

817 hydrothermal monazite: criteria for selection for samples for dating epigenetic hydrothermal ore

818 deposits: *Economic Geology*, v. 99, p. 1027-1035.

819 Seal, R.R., 2006, Sulfur Isotope Geochemistry of Sulfide Minerals: *Reviews in Mineralogy and*

820 *Geochemistry*, v. 61, p. 633-677.

821 Sharma, K.K., 2004, The Neoproterozoic Malani magmatism of the northwestern Indian shield:

822 implications for crust building processes: *Journal of Earth System Sciences*, v. 113, p. 795-807.

823 Sillitoe, R.H., 2003, Iron oxide-copper-gold deposits: An Andean view: *Mineralium Deposita*, v.

824 38, p. 787-812.

825 Singh, S.P., 1988, Sedimentation patterns of the Proterozoic Delhi Supergroup, northwestern

826 Rajasthan, India, and their tectonic implications: *Sedimentary Geology*, v. 58, p. 79-94.

827 Singh, Y.K., De Waele, B., Karmarkar, S., Sarkar, S., and Biswal, T.K., 2010, Tectonic setting of

828 the Balaream-Kui-Surpagla-Kengora granulites of the South Delhi Terrane of the Aravalli

829 Mobile Belt, NW India and its implication on correlation with the East African Orogen in the

830 Gondwana assembly: *Precambrian Research*, v. 183, p. 669-688.

831 Sinha-Roy, S., Malhotra, G., and Mohanty, M., 1998, *Geology of Rajasthan*. Geological Society of

832 India, Bangalore. 278 pp.

833 Torsvik, T.H., Carter, L.M., Ashwal, L.D., Bhushan, S.K., Pandit, M.K., and Jamtveit, B., 2001,

834 Rodinia refined or obscured: palaeomagnetism of the Malani Igneous Suite (NW India):

835 *Precambrian Research*, v. 108, p. 319-333.

836 van Lente, B., Ashwal, L.D., Pandit, M.K., Bowring, S.A., and Torsvik, T.H., 2009,

837 Neoproterozoic hydrothermally altered basaltic rocks from Rajasthan, northwest India:

838 implications for late Precambrian tectonic evolution of the Aravalli Craton: *Precambrian*

839 *Research*, v. 170, p. 202-222.

- 840 Vielreicher, N., Groves, D., McNaughton, N., and Fletcher, I., 2015, The timing of gold  
841 mineralization across the eastern Yilgarn craton using U–Pb geochronology of hydrothermal  
842 phosphate minerals: *Mineralium Deposita*, v. 50, p. 391-428.
- 843 Vijaya Rao, V., Rajendra Prasad, B., Reddy, P.R., and Tewari, H.C., 2000, Evolution of  
844 Proterozoic Aravalli Delhi Fold Belt in northwestern Indian Shield from seismic studies:  
845 *Tectonophysics*, v. 327, p. 109-130.
- 846 Wiedenbeck, M., and Goswami, J.N., 1994, An ion-probe single zircon Pb age from the Mewar  
847 Gneiss at Jhamarkotra, Rajasthan: *Geochimica et Cosmochimica Acta*, v. 58, p. 2135-2141.
- 848 Wiedenbeck, M., Goswami, J.N., and Roy, A.B., 1996, Stabilisation of the Aravalli craton of the  
849 north-western India at 2.5 Ga: an ion-microprobe zircon study: *Chemical Geology*, v. 129, p.  
850 325-340.
- 851 Williams, I.S., 1998, U-Th-Pb geochronology by ion microprobe: *Reviews in Economic Geology*,  
852 v. 7, p. 1-35.
- 853 Williams, M.L., Jercinovic, M.J., and Hetherington, C.J., 2007, Microprobe Monazite  
854 Geochronology: Understanding Geologic Processes by Integrating Composition and  
855 Chronology: *Annual Review of Earth and Planetary Sciences*, v. 35, p. 137-175.
- 856 Williams, P.J., Kendrick, M.A., and Xavier, R.P., 2010, Sources of ore fluid components in IOCG  
857 deposits, in Porter, T.M., e.d., *Hydrothermal iron oxide copper–gold & related deposits: a global  
858 perspective*, volume 2: Adelaide, PGC Publishing, p. 107-116.
- 859 Williams-Jones, A.E. and Migdisov, A.A., 2014, Experimental Constraints on the Transport and  
860 Deposition of Metals in Ore-Forming Hydrothermal Systems. *Society of Economic Geologists*,  
861 Inc. Special Publication, v. 18, p. 77-95.
- 862 Xavier, R.P., Wiedenbeck, M., Trumbull, R.B., Dreher, A.M., Monteiro, L.V.S., Rhede, D., Araújo,  
863 C.E.G., and Torresi, I., 2008, Tourmaline B-isotopes fingerprint marine evaporites as the source  
864 of high-salinity ore fluids in iron oxide-copper-gold deposits, Carajás Mineral province (Brazil):  
865 *Geology*, v. 36, p. 743-746.
- 866 Xiao, Y., Hoefs, J., and Kronz, A., 2005, Compositionally zoned Cl-rich amphiboles from North  
867 Dabie Shan, China: monitor of high-pressure metamorphic fluid/rock interaction processes:  
868 *Lithos*, v. 81, p. 279-295.
- 869 Yang, Y.H., Wu, F.Y., Yang, J.H., Chew, D.M., Xie, L.W., Chu, Z.Y., Zhang, Y.B., and Huang, C.,

2014, Sr and Nd isotopic compositions of apatite reference materials used in U-Th-Pb geochronology: *Chemical Geology*, v. 385, p. 35-55.

### Figure captions

Fig. 1 (a) Major tectonic units of India. (b) A simplified geological map of the Aravalli-Delhi Fold Belt, showing the major Precambrian lithotectonic units (modified after [Kaur et al., 2014](#)).

Fig. 2 (a) A simplified geological map of the Khetri Copper Belt (KCB), showing the distribution of Cu-(Au) deposits (modified after [Chen et al., 2015](#)); (b) and (c) Cross-sections of the Madhan-Kudhan and Kolihan deposits, respectively, showing the relationships between orebodies and host rocks (modified after [Knight et al., 2002](#)).

Fig. 3 Field (a to d) and hand specimen (e and h) photographs of selected rock types from the KCB. (a) Quartzite of the Alwar Group. Note that the quartzite has been altered to a reddish color. (b) Banded quartzite of the Alwar Group. The dark colored band is composed mainly of amphibole, whereas the light colored band is composed mainly of quartz. (c) Garnet-bearing quartzite of the Ajabgarh Group. Note that the garnet has been stretched and help to define the gneissosity of the rock. (d) Breccias between the Alwar and Ajabgarh Groups. (e) A sample of massive ore from the Madan-Kudan deposit, which mainly contains chalcopyrite, Ca-group amphibole and biotite. (f) A sample of massive ore from the Madan-Kudan deposit, which mainly contains pyrrhotite and Ca-group amphibole. (g) A sulfide-bearing vein cutting through the foliation of the quartzite. (h) Sulfide patches and disseminations in the quartzite distal to the main ore lenses.

Fig. 4 Photomicrographs of ores and altered host rocks from the KCB. (a) Magnetite and chalcopyrite from a massive ore sample. The chalcopyrite is interstitial to and

900 thus paragenetically later than the magnetite. (b) Sulfide veinlets following garnet  
 901 grain boundaries. (c) Sulfide-allanite veins overprinting cummingtonite and Ca-group  
 902 amphibole. (d) Scapolite crystals surrounded by sulfide minerals and biotite. (e)  
 903 Sulfide-biotite-chlorite veins passing through the quartzite hosting the ore. (f)  
 904 Randomly oriented cummingtonite crystals in garnet-bearing quartzite. (g) Randomly  
 905 oriented cummingtonite and Ca-group amphibole in quartzite. Note that some  
 906 cummingtonite crystals have been partially replaced by Ca-group amphibole. (h)  
 907 Quartzite partially replaced by biotite. (i) Quartzite partially replaced by chlorite.  
 908 Abbreviations: Aln-allanite, Amp-amphibole, Bt-biotite, Ccp-chalcopyrite,  
 909 Chl-chlorite, Cum-cummingtonite, Grt-garnet, Mgt-magnetite, Po-pyrrhotite,  
 910 Qz-quartz, Scp-Scapolite.

911

912 Fig. 5 A sketch map showing the locations of two monazite-(Ce)-bearing samples  
 913 from the 0 meter level of the Madhan-Kudhan mine.

914

915 Fig. 6 Photomicrographs (a to d) and BSE images (e and f) of minerals from sample  
 916 In-123. (a) Cummingtonite overprinted by later-stage magnetite. (b) and (c) The same  
 917 area under transmitted light and reflected light, respectively, showing that magnetite  
 918 was overprinted by later-stage sulfide minerals and biotite. (d) A cluster of  
 919 monazite-(Ce) crystals in association with sulfide minerals and biotite. (e) and (f)  
 920 Euhedral to subhedral monazite-(Ce) crystals. Note that some sulfide minerals occur  
 921 as inclusions in monazite-(Ce).

922 Abbreviation: Mnz-monazite-(Ce). Others are the same as in Fig. 4.

923

924 Fig. 7 Photomicrographs (a to d) and BSE images (e and f) of minerals from sample  
 925 In-125. (a) Cummingtonite crystals overprinted by later-stage magnetite. (b) and (c)  
 926 The same area under transmitted light and reflected light, respectively. The two  
 927 figures show that tourmaline contains many euhedral to subhedral magnetite  
 928 inclusions, and tourmaline and magnetite were overprinted by later-stage sulfide  
 929 minerals and biotite. (d) A subhedral monazite-(Ce) crystal occurs in contact with

930 biotite and, locally, magnetite. Some subhedral biotite crystals occur as inclusions in  
931 monazite-(Ce). (e) Subhedral monazite-(Ce) crystals in contact with chalcopyrite,  
932 biotite and quartz. (f) A large, euhedral monazite-(Ce) crystal in contact with  
933 chalcopyrite, biotite, quartz and, locally, zircon. This crystal hosts some inclusions of  
934 chalcopyrite and thorite.

935 Abbreviations: Thr-thorite, Tur-tourmaline, Zrn-zircon. Others are the same as in Figs.  
936 4 and 6.

937

938 Fig. 8 Photomicrographs (a to c) and BSE image (d) of minerals from sample In-103.  
939 (a) A subhedral tourmaline crystal in a biotite matrix. Some sulfide minerals occur in  
940 association with tourmaline. (b) and (c) Monazite-(Ce) clusters in the biotite matrix.  
941 Note that the monazite-(Ce) crystals have highly variable sizes and shapes within  
942 individual clusters. (d) A subhedral monazite-(Ce) crystal containing an inclusion of  
943 pyrrhotite.

944 Abbreviations are the same as in Figs. 4 and 6.

945

946 Fig. 9 Photomicrographs (a to c) and BSE image (d) of minerals from sample In-192.  
947 (a) Magnetite overprinted by later-stage sulfide minerals and chlorite. (b) Scapolite  
948 crystals in contact with magnetite and pyrrhotite. (c) A monazite-(Ce) crystal in  
949 contact with chlorite and pyrrhotite. The monazite-(Ce) crystal contains an inclusion  
950 of pyrrhotite. (d) A large, irregularly shaped monazite-(Ce) crystal and several tiny  
951 monazite-(Ce) crystals in association with chlorite, pyrrhotite and quartz. Several  
952 pyrrhotite grains occur as inclusions in the large monazite-(Ce) crystal. (e) An  
953 irregularly shaped monazite-(Ce) crystal in contact with sulfide minerals, quartz and  
954 chlorite. This crystal has been partially replaced by pyrrhotite and some unidentified  
955 silicate minerals. (f) A rounded monazite-(Ce) crystal enclosed by pyrrhotite. (g) A  
956 sub-rounded monazite-(Ce) crystal enclosed by pyrrhotite. Note that this crystal has a  
957 discontinuous bright film near the grain margin. Quartz occurs as inclusion in  
958 monazite-(Ce). (h) A sub-rounded monazite-(Ce) crystal enclosed by pyrrhotite. This  
959 crystal also has a bright film near the grain margin.



Abbreviations are the same as in Figs. 4 and 6.

Fig. 10 (a) A plot of the composition of monazite-(Ce) in terms of the parameters  $4*(Th + U + Si)$  and  $4*(REE + Y + P)$ . The labeled dashed lines illustrate the effects on the composition of the substitution of brabantite  $Ca(Th, U)REE_{-2}$  vs. huttonite  $(Th, U)SiREE_{-1}P_{-1}$  into the structure. (b) A histogram showing the content of  $ThO_2$  in monazite-(Ce) from samples In-123, In-125, In-103 and Type 1 and 2 Monazite-(Ce) from sample In-192. Also shown are data for the composition of metamorphic monazite-(Ce) from the southern part of Aravalli-Delhi Fold Belt are also shown for comparison (the data are from [Bhowmik et al., 2010](#); [Just et al., 2011](#) and [Ozha et al., 2016](#)).

Fig. 11 U-Pb concordia diagrams for (a) monazite-(Ce) from sample In-123; (b) monazite-(Ce) from sample In-125; (c) monazite-(Ce) from sample In-103; (d) Type 1 monazite-(Ce) from sample In-192; and (e) Type 2 monazite-(Ce) from sample In-192. Note that the gray ellipses in (c) and (d) were not included in the age calculation. See text for detailed explanations.

Fig. 12 (a) A plot of  $^{147}Sm/^{144}Nd$  vs.  $^{143}Nd/^{144}Nd$  for monazite-(Ce) from samples In-123, In-125, In-103 and Type 1 monazite-(Ce) from sample In-192. (b) Histograms showing  $\epsilon_{Nd}(t=835Ma)$  values for the monazite-(Ce) in a. The ranges of  $\epsilon_{Nd}$  values at 835 Ma for regional Paleoproterozoic intrusions are also shown for comparison (light grey areas). The Sm-Nd isotopic data for the regional Paleoproterozoic intrusions are from [Kaur et al., 2007, 2009, 2011b, 2012, 2013](#).

Fig. 13 An event-time chart summarizing isotopic ages for collision-related metamorphism, post-collisional magmatism, regional metasomatism and Cu-(Au) mineralization in the Aravalli-Delhi Fold Belt. The following were the sources for the data: 1. [Ozha et al., 2016](#); 2. [Hazarika et al., 2013](#); 3. [Bhowmik et al., 2010](#); 4. [Pant et al., 2008](#); 5. [van Lente et al., 2009](#); 6. [Just et al., 2011](#); 7. [Singh et al., 2010](#); 8. [Deb et](#)

990 al., 2001; 9. Knight et al., 2002; 10. Kaur et al., 2013; 11. this study.

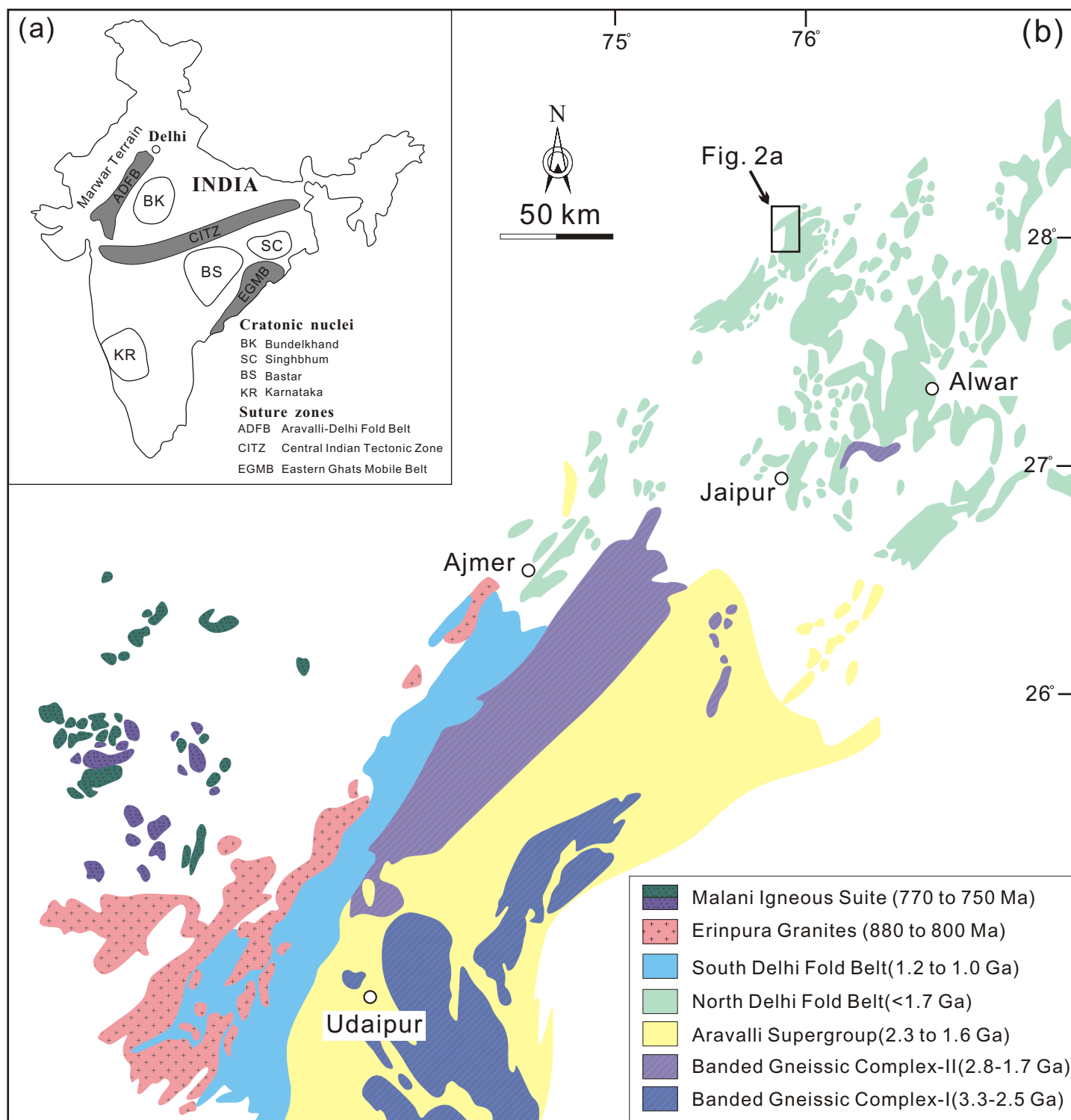


Fig. 1

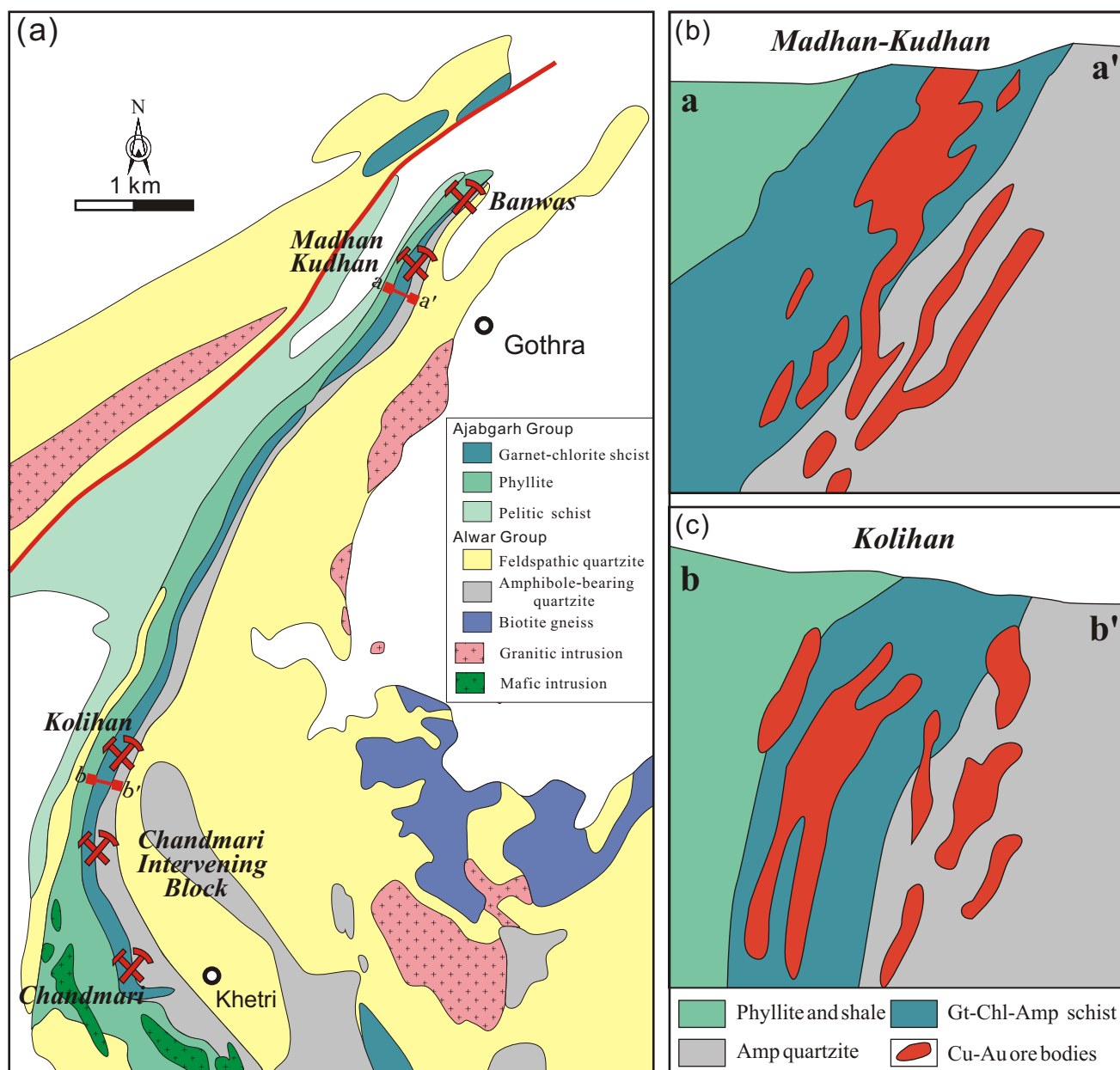
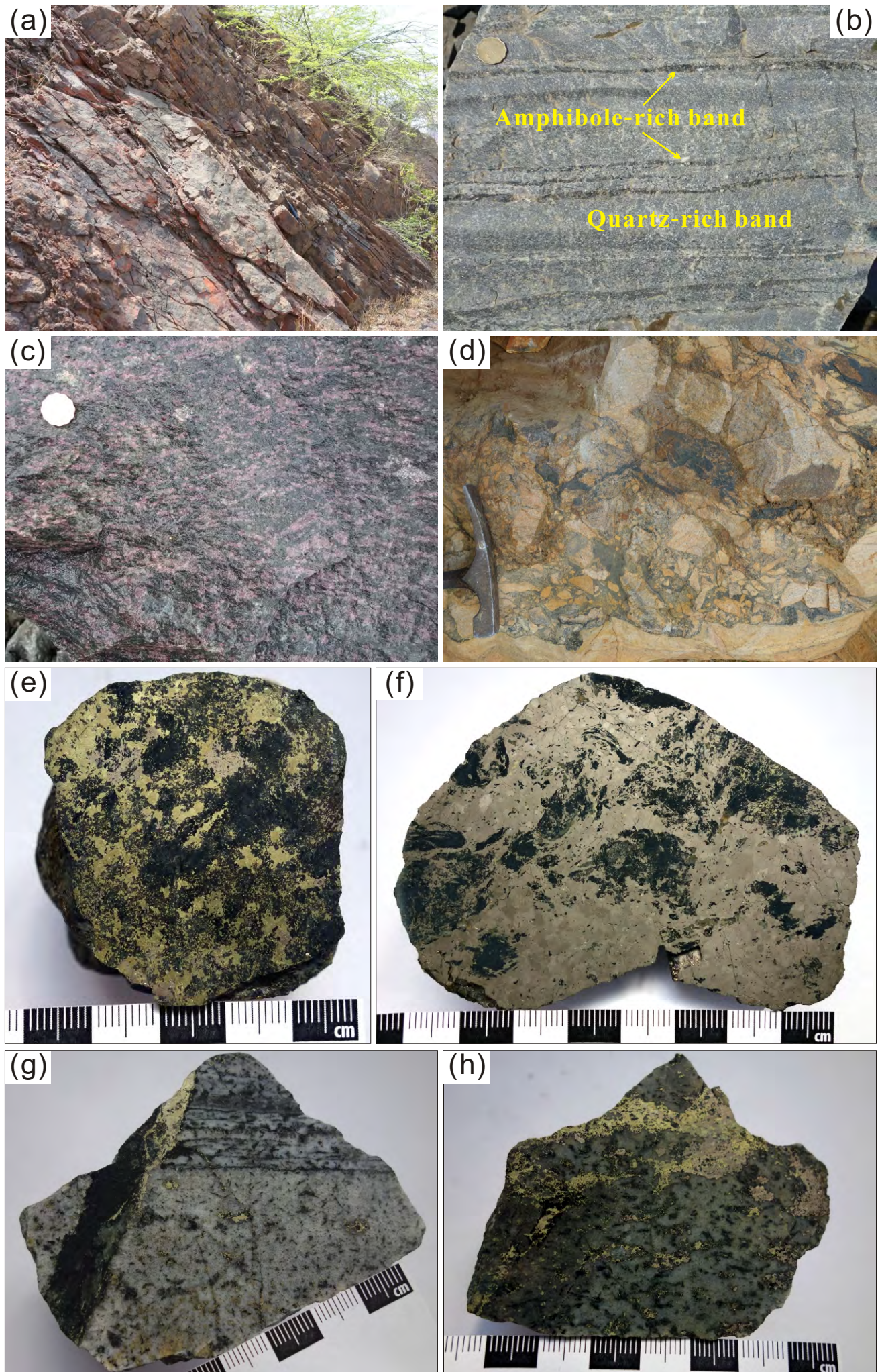


Fig. 2





**Fig. 3**



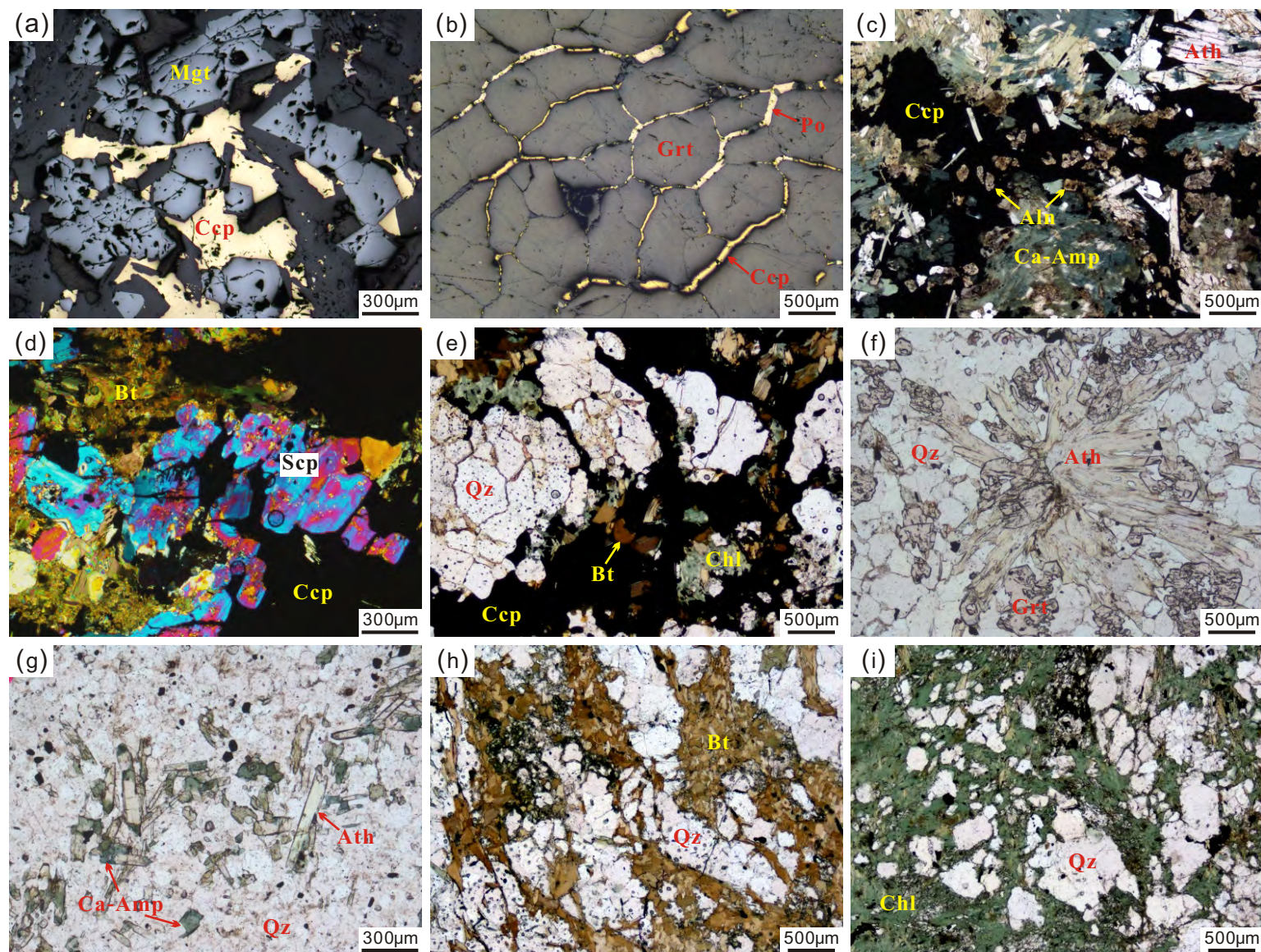


Fig. 4



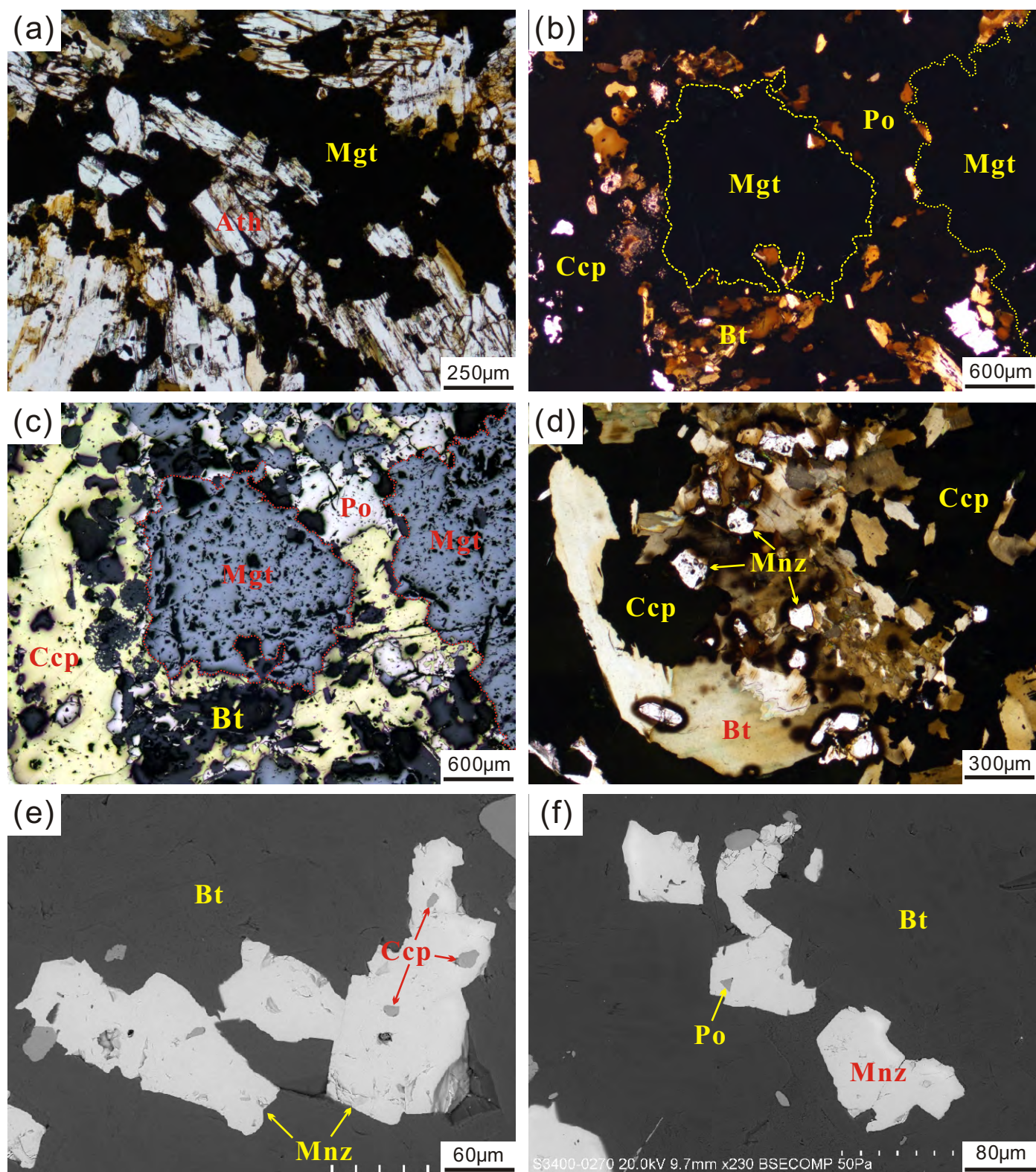


Fig. 5



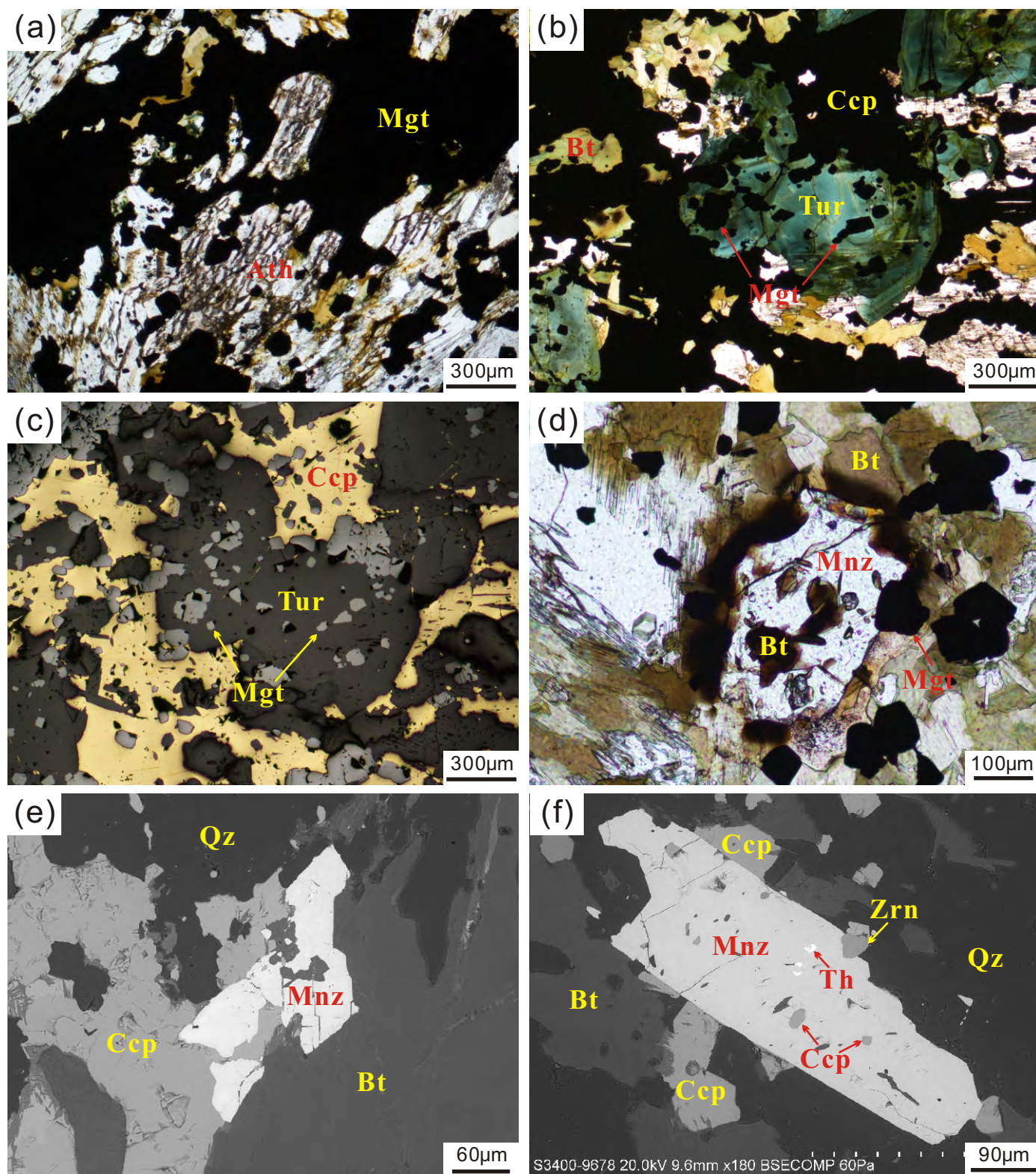


Fig. 6



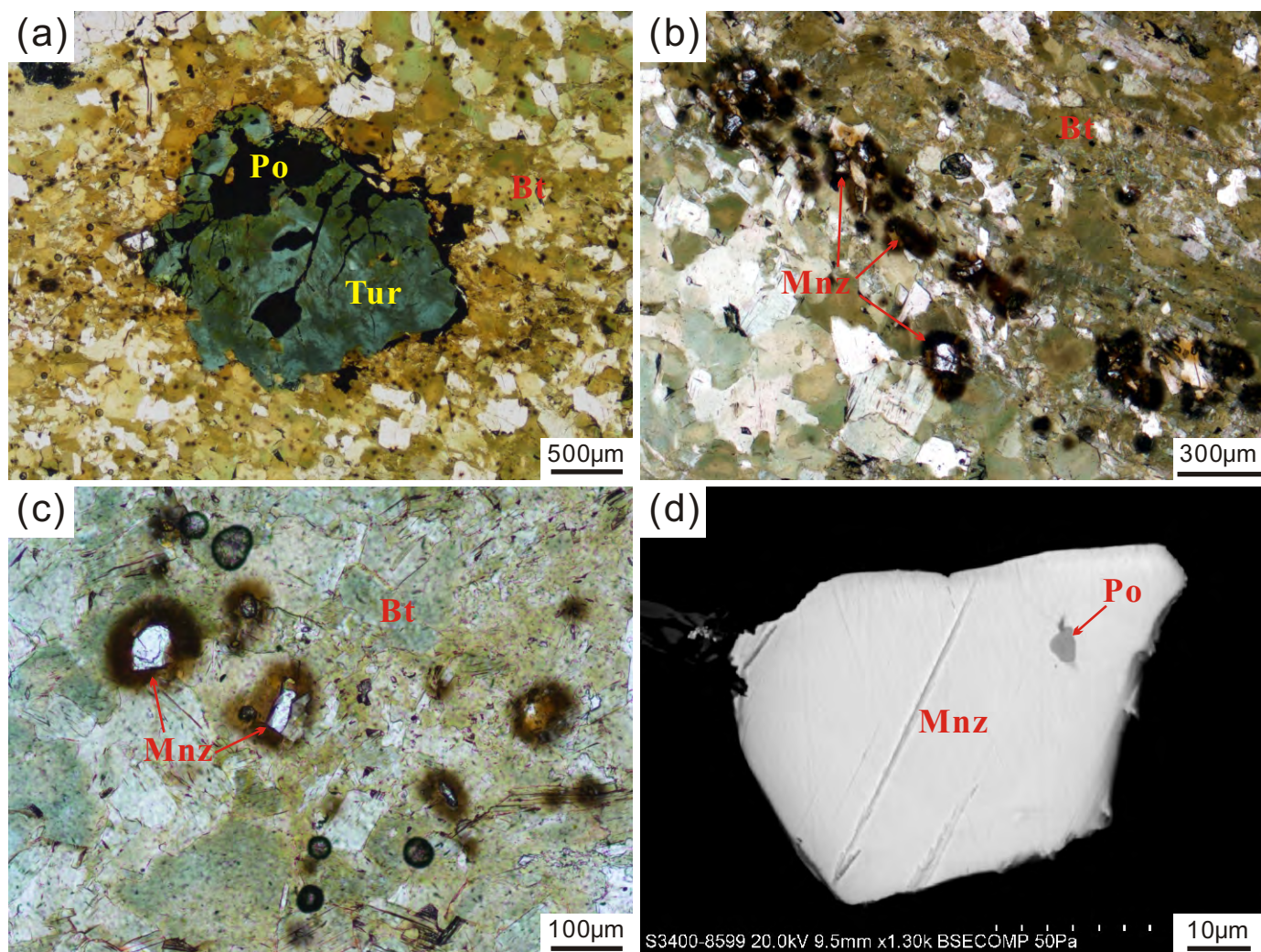


Fig. 7

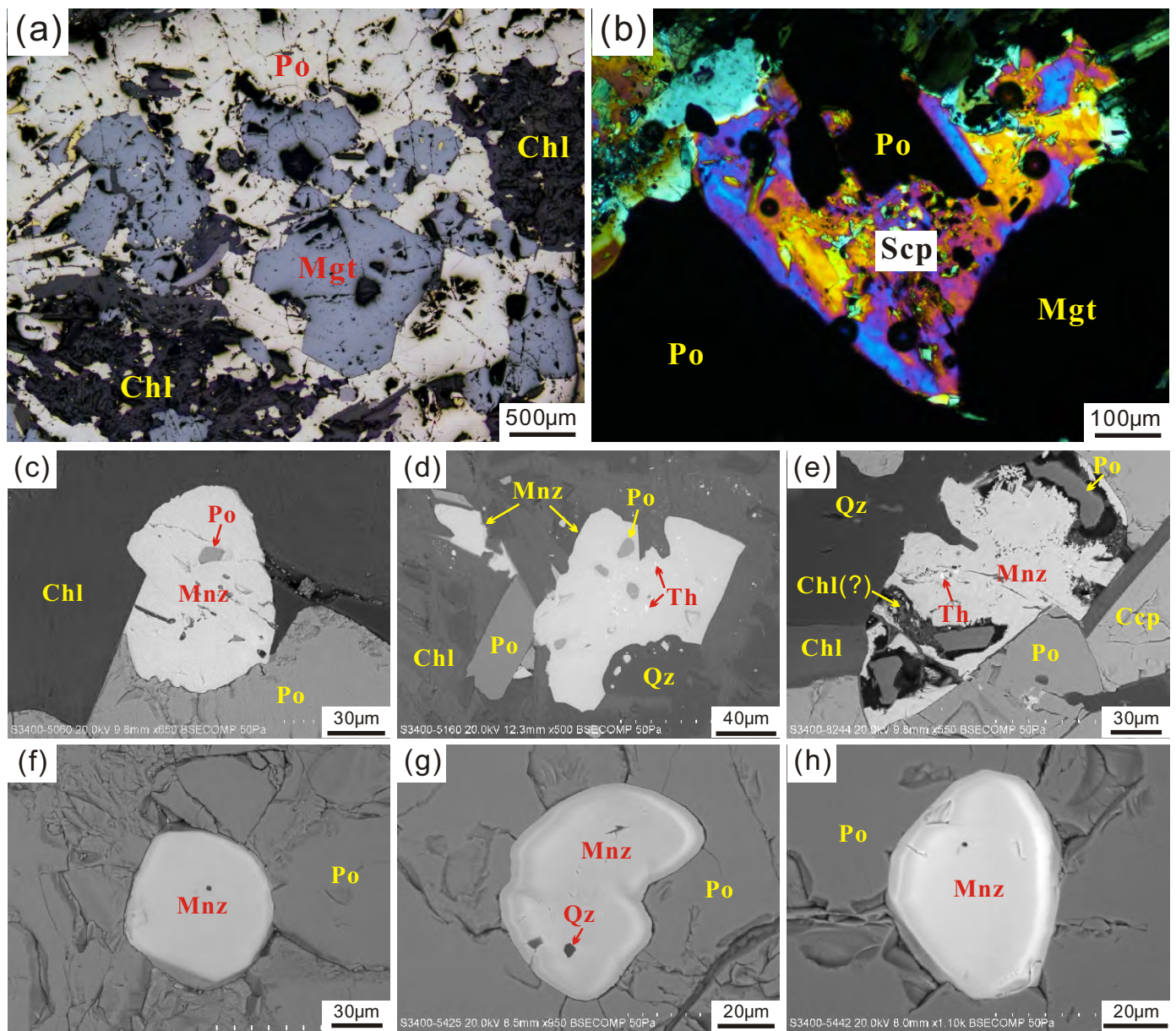


Fig. 8

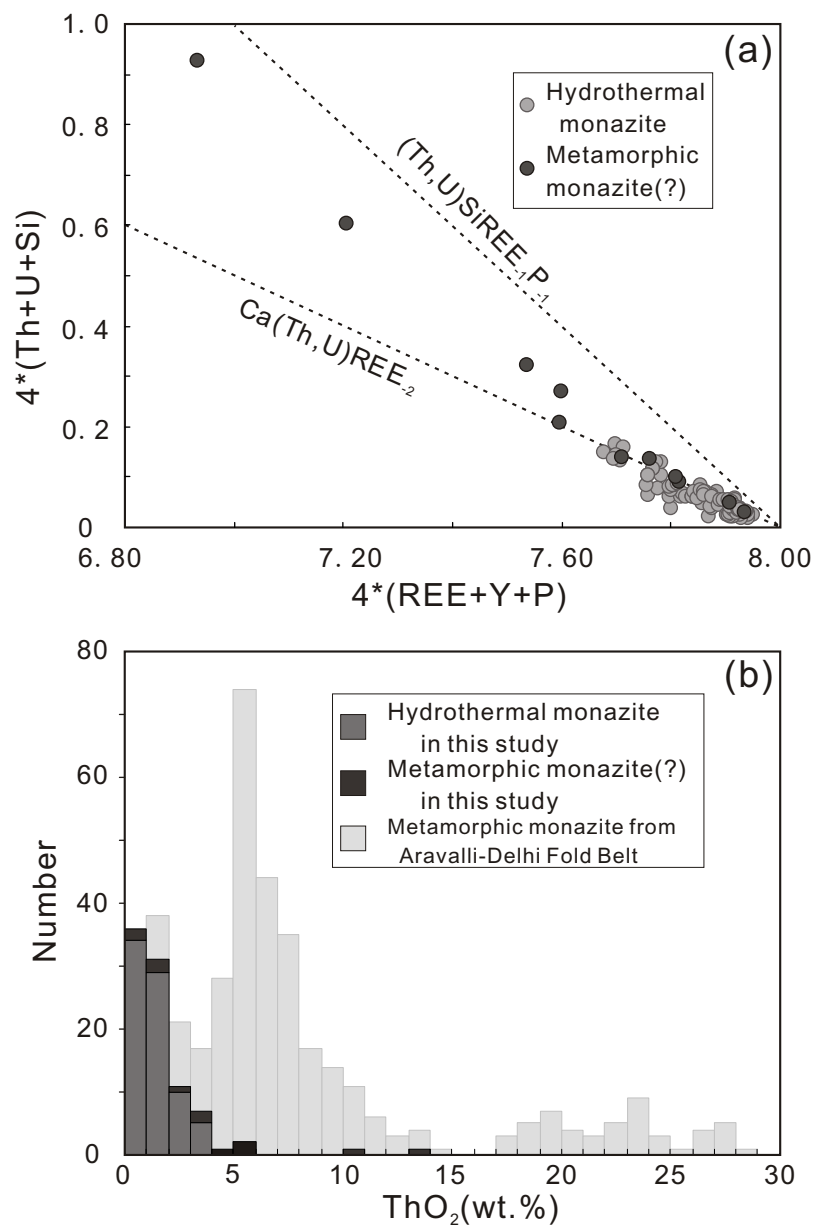


Fig. 9



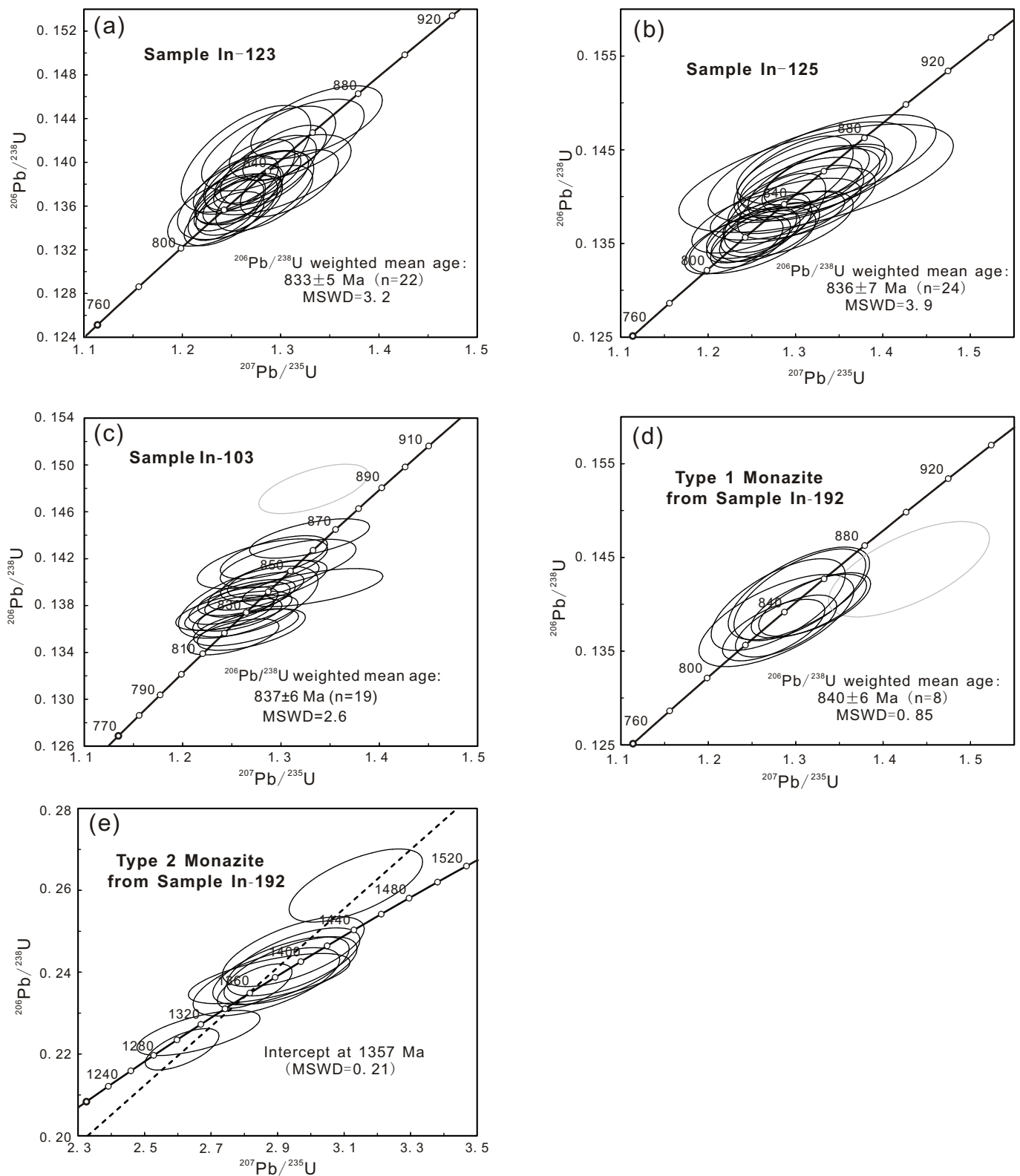


Fig. 10

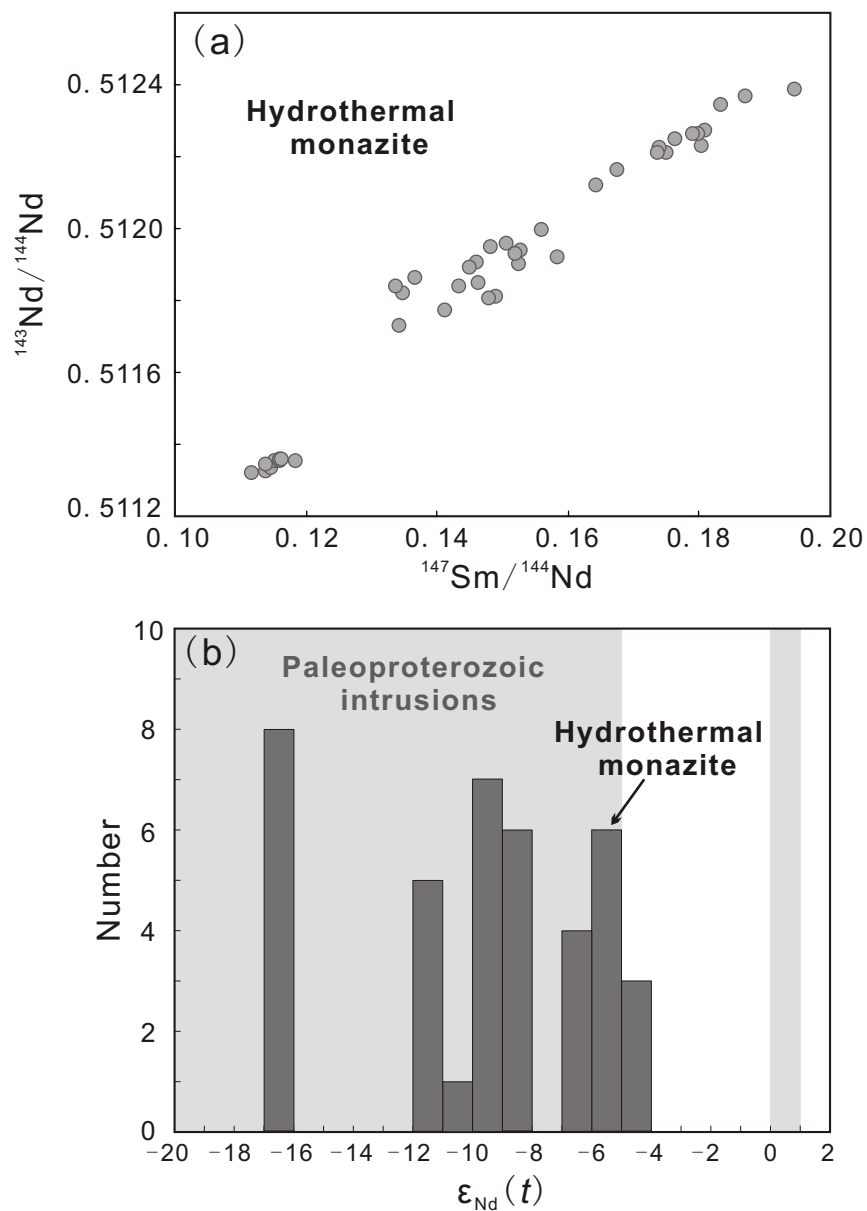


Fig. 11

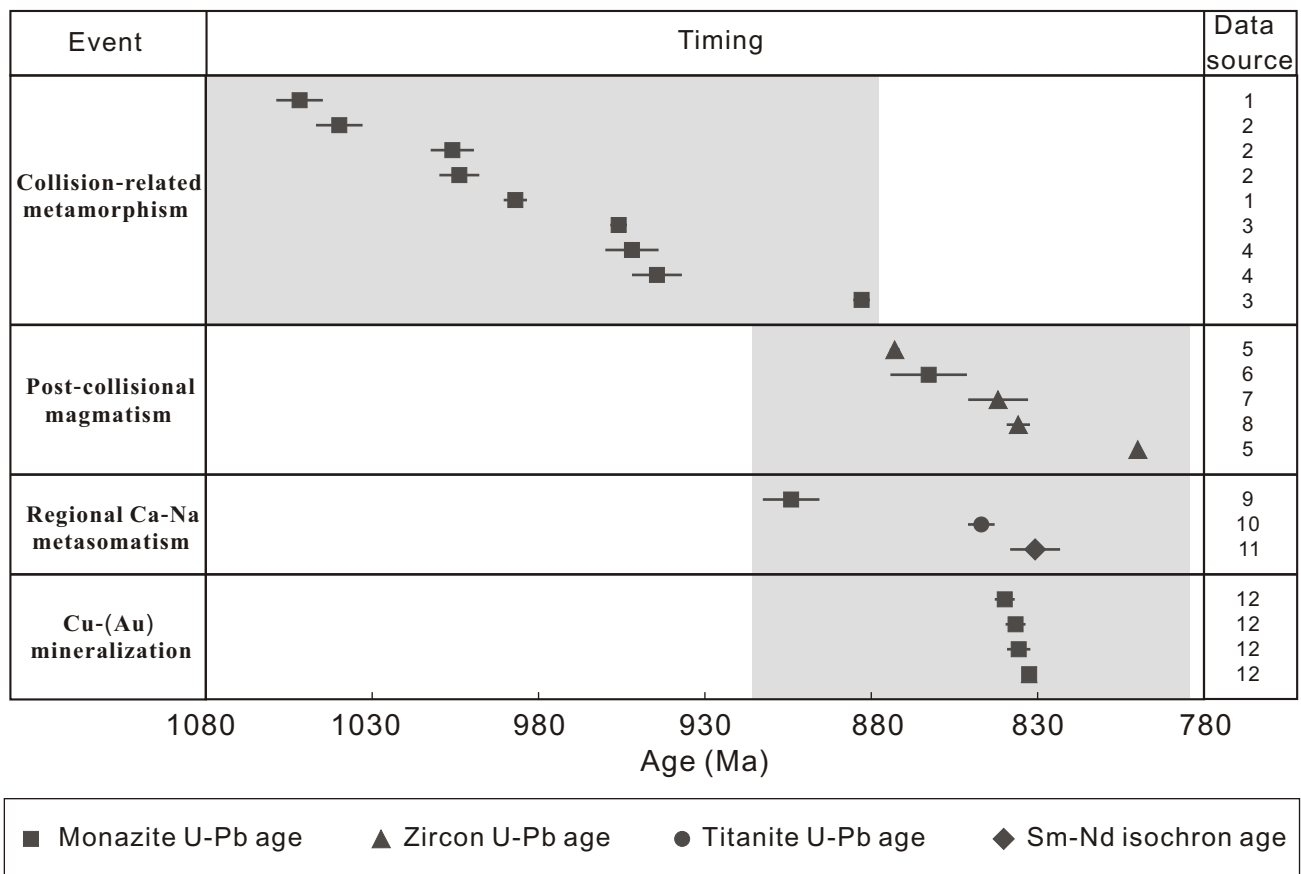


Fig. 11